

# Single Vortex Dynamics in High Temperature Bose-Einstein Condensates

Samuel J. Rooney

September 2009

A dissertation submitted in partial fulfillment  
for the degree of Bachelor of Science with Honours  
in Combined Physics and Mathematics



## Abstract

We present the first numerical investigation of three dimensional vortex dynamics in a high temperature Bose-Einstein condensate, using a stochastic theory accounting for both diffusive and dissipative vortex decay processes. At temperatures approaching the critical temperature, there is a significant thermal fraction and interactions between the condensate and thermal cloud can not be neglected. We use a projected stochastic Gross-Pitaevskii equation based on c-field techniques to account for such interactions which are inherently stochastic.

We investigate the vortex dynamics over a range of temperatures and condensate geometries. To undertake such a complete investigation we derived a simple method of predicting the parameters used in the stochastic Gross-Pitaevskii equation such that the number of atoms in the total system are constrained. By using a Hartree-Fock approximation of the interactions, we find a quick and accurate method in which we are confident in controlling the system prior to simulations. Due to the accuracy of the parameters we use, this is the most complete treatment of damping in the stochastic Gross-Pitaevskii equation that has been used in numerical calculations to date.

In contrast to treatments involving purely dissipative processes, we find single vortex decay is very complex involving a range of dissipative and diffusive dominated decay. We find new physics based on diffusive vortex decay, arising from the noise incorporated in the stochastic Gross-Pitaevskii equation. We observe that the role of diffusion leads to considerably different vortex decay, over a range of temperatures, to that previously reported using non stochastic methods [30]. We observe most interestingly that the form of the vortex decay is universal over condensate dimensionality.

# Acknowledgements

Firstly I must thank my supervisor, Dr Ashton Bradley, for all he has done for me this year. I will always appreciate his enthusiasm, willingness and ability to impart his wealth of knowledge, and most importantly the support he has given me throughout this year. In the same way I thank Dr Blair Blakie, who also helped with my supervision. Without the help and support of Ashton and Blair, none of the work presented here would have been possible, so I thank them both greatly.

To all the Honours students this year, thanks for making room 509 such an enjoyable place, especially over the last month during the writing period. I never thought it would be such fun being in the physics department at four in the morning!

Of course I thank my family, my parents Liz and Owen, Sarah and my Grandma, for all their love and support in everything I have endeavored not only this year, but throughout my life.

Finally to Emma, for all your love and support over the last five years. Thank you for always being there for me.

# Contents

|          |  |          |
|----------|--|----------|
| <b>1</b> | <b>Introduction</b>  | <b>1</b> |
| <b>2</b> | <b>Background</b>  | <b>3</b> |
| 2.1      | Bose-Einstein Condensation . . . . .                             | 3        |
| 2.2      | Zero Temperature Theory . . . . .                                | 4        |
| 2.3      | Vortices . . . . .   | 4        |
| 2.3.1    | Superfluid Helium . . . . .                                      | 4        |
| 2.3.2    | Vortices in Bose-Einstein Condensation . . . . .                 | 4        |
| 2.3.3    | Vortex Stability . . . . .                                       | 5        |
| 2.3.4    | Kelvin Modes . . . . .   | 6        |
| 2.4      | High Temperature Theory . . . . .                                | 6        |
| 2.4.1    | C-Field Methods . . . . .  | 7        |
| 2.4.2    | Vortices in High Temperature Bose-Einstein Condensates . . . . . | 7        |
| <b>3</b> | <b>C-Field Formalism</b>   | <b>9</b> |
| 3.1      | Effective Field Theory . . . . .                                 | 9        |
| 3.2      | Projection into the Classical Field Region . . . . .             | 11       |
| 3.2.1    | Theory of the Projector Operator . . . . .                       | 11       |
| 3.2.2    | Full Hamiltonian . . . . .                                       | 12       |
| 3.2.3    | C-Field Methods . . . . .  | 13       |
| 3.3      | Wigner Formalism . . . . .                                       | 14       |
| 3.3.1    | Overview of Phase-Space Methods . . . . .                        | 14       |
| 3.3.2    | Coherent States . . . . .  | 14       |
| 3.3.3    | Wigner Representation of a Single Quantum Mode . . . . .         | 15       |
| 3.3.4    | Wigner Representation of the Quantum Field . . . . .             | 16       |
| 3.3.5    | The Truncated Wigner Approximation . . . . .                     | 17       |
| 3.4      | The Projected Gross-Pitaevskii Equation . . . . .                | 18       |
| 3.5      | The Stochastic Gross-Pitaevskii Equation . . . . .               | 18       |
| 3.5.1    | The Master Equation . . . . .                                    | 19       |
| 3.5.2    | The Stochastic Gross-Pitaevskii Equation . . . . .               | 19       |
| 3.5.3    | Growth and Scattering Processes . . . . .                        | 20       |
| 3.5.4    | Simple Growth SGPE . . . . .                                     | 21       |

|          |  |           |
|----------|--|-----------|
| <b>4</b> | <b>SGPE Parameters</b>                                   | <b>23</b> |
| 4.1      | Overview . . . . .                                       | 23        |
| 4.2      | Methods . . . . .  | 24        |
|          | 4.2.1 Chemical Potential . . . . .                       | 24        |
|          | 4.2.2 Energy Cutoff . . . . .                            | 25        |
| 4.3      | Results . . . . .  | 26        |
|          | 4.3.1 Hatree-Fock Results . . . . .                      | 26        |
|          | 4.3.2 SGPE Results . . . . .                             | 27        |
| 4.4      | Limitations . . . . .                                    | 32        |
| 4.5      | Summary . . . . .  | 32        |
| <b>5</b> | <b>Numerical Methods</b>                                 | <b>33</b> |
| 5.1      | Vortex States . . . . .                                  | 33        |
| 5.2      | Vortex Detection . . . . .                               | 34        |
| 5.3      | Mean First Exit Time . . . . .                           | 36        |
| 5.4      | Convergence . . . . .                                    | 37        |
| 5.5      | Simulation Parameters . . . . .                          | 38        |
| 5.6      | Computational Requirements . . . . .                     | 39        |
| <b>6</b> | <b>Results</b>   | <b>40</b> |
| 6.1      | Observation of Lifetime . . . . .                        | 40        |
| 6.2      | Ensemble Averaging and Statistical Convergence . . . . . | 43        |
| 6.3      | Effects of Temperature . . . . .                         | 44        |
|          | 6.3.1 Angular Momentum . . . . .                         | 44        |
|          | 6.3.2 Mean First Exit Time . . . . .                     | 46        |
| 6.4      | Effects of Geometry . . . . .                            | 49        |
|          | 6.4.1 Mean First Exit Time . . . . .                     | 49        |
|          | 6.4.2 Angular Momentum . . . . .                         | 51        |
|          | 6.4.3 Mean Vortex Radius . . . . .                       | 52        |
|          | 6.4.4 Temperature Dependence of All Geometries . . . . . | 53        |
| <b>7</b> | <b>Conclusion</b>  | <b>54</b> |
| 7.1      | Summary . . . . .  | 54        |
| 7.2      | Directions for Future Research . . . . .                 | 55        |
| <b>A</b> | <b>Supplementary Figures</b>                             | <b>56</b> |

# Chapter 1

## Introduction

The theoretical treatment of Bose-Einstein condensation at zero temperature has been tremendously successful in correctly predicting experimental observations via the Gross-Pitaevskii equation [14]. However at temperatures approaching the critical temperature, a fully mean field description of the system becomes inadequate and the Gross-Pitaevskii equation will not account for all the physical processes present with a substantial thermal component.

In high temperature Bose-Einstein condensation where the temperature is larger than the single particle energy, the presence of a large thermal cloud means coupling processes between thermal atoms and the condensate can not be neglected. Accounting for scattering processes between the thermal cloud and condensate leads to a fully stochastic theory known as the stochastic Gross-Pitaevskii equation (SGPE), which arises from the  $c$ -field formalism [5]. The SGPE formalism has been presented in rigorous detail [25, 10], however there is a current lack of numerical investigation using the theory.

The achievement of Bose-Einstein condensation in a dilute gas [2] sparked massive interest in the field of ultra-cold atoms. In particular as the phenomena of superfluidity is intimately connected with Bose-Einstein condensation, there is scope to test the behavior of superfluids using the weakly interacting dilute gas. The dynamics of vortices in zero temperature Bose-Einstein condensation have been well described theoretically due to the success of the Gross-Pitaevskii equation [23]. However, the stability and dynamics of vortices in a high temperature Bose-Einstein condensate are not fully understood.

Jackson *et al.* [30] have investigated vortex dynamics at finite temperature using the Zaremba-Nikuni-Griffin (ZNG) formalism, where they claim to have the first microscopic simulations which fully account for the dynamics of an inhomogeneous thermal cloud. However ZNG theory only accounts for dissipation and is not formally a stochastic theory, yet at temperatures approaching the critical temperature the role of fluctuations will be increasingly important. A full description of the interactions must account for vortex decay due to diffusion as well as dissipation (see figure 1.1 for an explanation of the different decay processes). The SGPE accounts for both diffusive and dissipative processes, and a full numerical investigation of this regime has not been seen before using such a sophisticated theory. Thus the vortex dynamics in high temperature Bose-Einstein condensate is an interesting regime

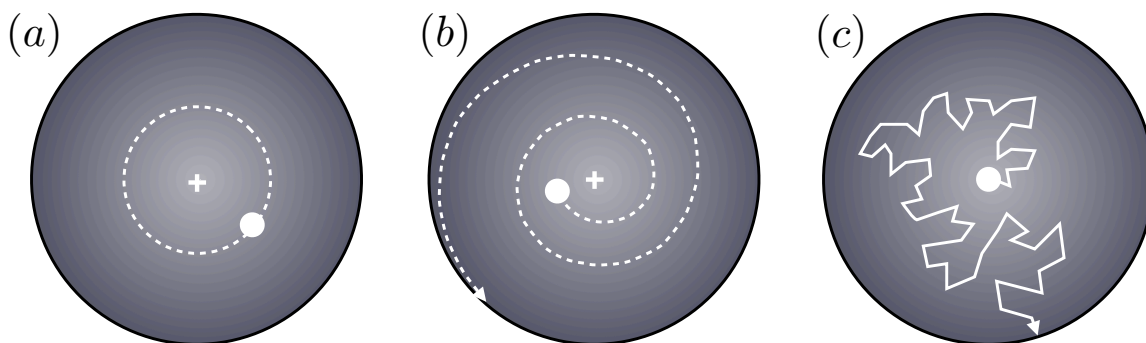


Figure 1.1: Schematic showing the difference between the various vortex decay processes. (a) In the presence of no dissipation, a single vortex follows trajectories of constant radius about the centre of the condensate. (b) At finite temperatures, the presence of a thermal cloud creates a dissipative mechanism. In the case of purely *dissipative* decay, an off centered vortex will decay to the edge of the condensate in a very regular spiral. (c) *Diffusive* dominated decay caused by thermal fluctuations leads to largely random vortex motion, where fluctuations can kick the vortex in any direction. We call a vortex that will decay to the boundary and have a finite lifetime *unstable*.

in which to test SGPE theory.

The aims of this research are:

1. In order to numerically investigate a wide range of regimes, the choice of SGPE parameters is crucial to be able to control the system. As this is the first time the SGPE has been used in such an investigation, we aim to find a quick and simple way of predicting a good choice of SGPE parameters.
2. We aim to understand the effect that thermal fluctuations have on single vortex decay in a qualitative manner. To do so we investigate a wide regime of single vortex dynamics using the SGPE over a range of temperatures and condensate geometries. We also aim to make quantitative predictions of the lifetime of a single vortex in realistic experimental scenarios.

# Chapter 2

## Background

### 2.1 Bose-Einstein Condensation

Bose-Einstein condensation was first predicted by Einstein in 1924 based on the work of Bose on the statistics of photons. This phenomena is based on the fact that Bosons are indistinguishable particles which, in thermal equilibrium at temperature  $T$ , obey Bose-Einstein distribution

$$n_{\text{BE}}(\epsilon) = \frac{1}{e^{(\epsilon-\mu)/k_{\text{B}}T} - 1}, \quad (2.1)$$

which gives the number of particles in a state with energy  $\epsilon$ , where the chemical potential  $\mu$  gives a constraint on the total number of particles in the system. The Bose-Einstein distribution says that at a critical temperature  $T_c$ , the ground state occupation  $n_0$  can become macroscopic when the chemical potential  $\mu$  approaches the lowest energy level  $\epsilon_0$ . This can be achieved by cooling the system while holding the number of atoms constant. The system has a Bose-Einstein condensate when the ground state becomes macroscopically occupied, which will occur when the thermal de Broglie wavelength becomes comparable to the mean interparticle spacing. This sets the critical temperature for Bose-Einstein condensation,  $T_c$ , and for a harmonically trapped gas this is [14]

$$k_{\text{B}}T_c = 0.94\hbar\bar{\omega}N^{1/3}, \quad (2.2)$$

where  $\bar{\omega} = (\omega_x\omega_y\omega_z)^{1/3}$  is the geometric average of the trapping frequencies.

Bose-Einstein condensation was first observed experimentally at JILA [2] in 1995, where a dilute gas of rubidium atoms were magnetically trapped and cooled to temperatures of the order of fractions of micro-Kelvins. This experimental observation sparked major interest in the field of ultra-cold atoms as Bose-Einstein condensation provides a unique field to explore complex quantum phenomena on a macroscopic scale.



## 2.2 Zero Temperature Theory

Bose-Einstein condensation is a theoretically appealing field due to the highly Bose-degenerate nature of the system. This degeneracy means that valid approximations can be made to the full many body quantum field theory describing all the particles in the system, to create more tractable theories.

The main tool used to describe Bose-Einstein condensation is the Gross-Pitaevskii equation [14]

$$i\hbar \frac{\partial \psi(\mathbf{x}, t)}{\partial t} = -\frac{\hbar^2}{2m} \nabla^2 \psi(\mathbf{x}, t) + V_0(\mathbf{x}, t) \psi(\mathbf{x}, t) + u |\psi(\mathbf{x}, t)|^2 \psi(\mathbf{x}, t), \quad (2.3)$$

where  $V_0(\mathbf{x}, t)$  is an external potential. The parameter  $u$  determines the interparticle interactions and is related to the scattering length  $a_s$  by

$$u = \frac{4\pi a_s \hbar^2}{m}. \quad (2.4)$$

The Gross-Pitaevskii equation is a nonlinear Schrödinger equation which gives a mean field description of the macroscopic wave function of the Bose-Einstein condensate. It gives an excellent description of Bose-Einstein condensation at zero temperature [14], since in this case all particles are in a single state described by the order parameter  $\psi(\mathbf{x}, t)$ . Hence the system is well described by simply the condensate wave function, so a mean field description is valid.

## 2.3 Vortices

### 2.3.1 Superfluid Helium

The earliest example of Bose-Einstein condensation was liquid  $^4\text{He}$ , which below the lambda point becomes a superfluid with many remarkable properties [17]. In 1938, London suggested that the superfluid component of He II was of the form of a Bose-Einstein condensate, as at very low temperatures the density of the superfluid component approaches the total density of the entire liquid. As He II is strongly interacting, it prevents a large condensate fraction from forming which provides difficulty in studying the superfluid component as the normal component dominates. The observation of Bose-Einstein condensation in dilute gases provides a setting in which superfluid behavior can be observed, as the interactions are much weaker in an alkali gas. Hence the condensed gas is an appealing regime in which to study superfluidity.

### 2.3.2 Vortices in Bose-Einstein Condensation

Vortices are topological defects observed in superfluids where the fluid rotates about the vortex at a speed inversely proportional to its radius. Similarly to a superfluid, circulation

in a Bose-Einstein condensed gas must be quantized. In the mean field description of Bose-Einstein condensation using the Gross-Pitaevskii equation, the single particle wave function represents the condensate. This wave function can be written in terms of its amplitude and phase by

$$\psi(\mathbf{x}, t) = |\psi(\mathbf{x}, t)|e^{i\theta(\mathbf{x}, t)}. \quad (2.5)$$

The condensate wave function must be single valued, but the phase is only defined up to multiples of  $2\pi$ .

The velocity flow of the condensate is defined by

$$\mathbf{v} = \frac{\hbar}{m} \nabla \theta(\mathbf{x}, t), \quad (2.6)$$

thus the phase acts as a velocity potential meaning that the condensate flow is irrotational

$$\nabla \times \mathbf{v} = 0. \quad (2.7)$$

Using the condensate velocity, it follows that the condensate circulation is quantized in units of  $h/m$

$$\oint \mathbf{v} \cdot d\mathbf{l} = n \frac{h}{m}. \quad (2.8)$$

The fact that the condensate flow is irrotational means that the condensate can not support a rigid-body rotation. However a Bose-Einstein condensate can support angular momentum through the presence of vortices, which represent one of the most characteristic features of superfluidity. A vortex is characterized by a line of zero density with a phase circulation of  $2\pi n$  about this line.

Vortices in Bose-Einstein condensation are an experimentally realized phenomena, and were first observed experimentally in Bose-Einstein condensation in 1999 at JILA [32]

### 2.3.3 Vortex Stability

The issue of vortex stability and the role of dissipation has been an issue of much debate. The ground state of a non-rotating Bose-Einstein condensate is vortex free so the presence of a vortex means the condensate is in an excited state [21, 23, 37]. However the system is metastable in that if there is an absence of any dissipation, the vortex will follow trajectories of constant energy remaining inside the condensate [38] (see figure 1.1). However in the presence of dissipation, a vortex state will be unstable as there is some mechanism to transfer the system to the lower energy vortex free ground state [37]. This effect has been realized experimentally by Anderson *et al.* [1] where they observed vortex precession where the vortex spirals out of the condensate. The interaction between the vortex and a thermal cloud was investigated by Fedichev and Shlyapnikov [20], where they discuss the dissipation of energy from the condensate to the thermal cloud. At temperatures approaching the critical

temperature  $T_c$ , there will be a large thermal component which will give a mechanism for dissipation of energy from the condensate to the thermal cloud creating vortex decay. The effect of a large thermal cloud on vortex decay is an interesting issue where there is currently no adequate complete description, largely because the Gross-Pitaevskii equation will not account for all the incoherent physical processes which will be present.

### 2.3.4 Kelvin Modes

Quantized vortex lines can support long-wavelength helical traveling waves known as Kelvin waves. In Bose-Einstein condensation these modes obey the well known Kelvin dispersion relation [22]

$$\omega_k \approx \frac{\hbar k^2}{2M} \ln \left( \frac{1}{|k|\xi} \right), \quad (2.9)$$

where  $k$  is the wave number along the vortex axis with the absolute value included to allow propagation of waves in either direction, and  $\xi$  is the vortex-core size. These Kelvin modes have been observed experimentally in an elongated cigar trap [12]. In a Kelvin mode, each element of the vortex core undergoes a circular orbit in the opposite direction to that of the circulating velocity of the vortex line. If enough Kelvin modes are active, the combination of these helical waves cause the vortex to bend which creates instability. In the case of a vortex in a dilute trapped Bose-Einstein condensate, the number of accessible Kelvin modes decreases as the condensate geometry becomes more two dimensional. This means that if geometry has any effect on vortex decay at high temperature, it is reasonable to expect the vortex decay rate will increase as the geometry becomes more spherical. However this has not been tested theoretically or experimentally.

## 2.4 High Temperature Theory

The Gross-Pitaevskii equation gives a good description of Bose-Einstein condensation at zero temperature as the approximation that the entire system can be described by a single wave function is valid. However as the temperature of the system becomes higher, there will be an increasingly significant thermal cloud. The Gross-Pitaevskii equation only deals with interparticle interactions from Bose condensed particles, hence it fails to provide an adequate description of a system in which incoherent and spontaneous processes are important. Such processes are present when a sizable thermal cloud exists.

The temperature range at which the thermal cloud becomes significant, so that the interaction between the condensate and thermal atoms is important, is classified as the high temperature regime. This occurs when the temperature of the system is significant compared to the single particle energies of the trapping potential. For a harmonic potential with frequency  $\omega$  as usually found in Bose-Einstein condensed systems, the criteria is

$$\hbar\omega \ll k_B T, \quad (2.10)$$

which generally consists of temperatures in the range  $0.6T_c < T$ .

In order to treat high temperature Bose-Einstein condensation, a theoretical description is required that necessarily includes the physics of spontaneous and incoherent processes.

### 2.4.1 C-Field Methods

The most complete theory that treats the high temperature regime involves techniques known generically as *c-field* methods [5]. This formalism utilizes the fact that even as temperatures become larger than even the critical temperature, there is still significant population of the lowest energy modes. When this occupation is larger than one quantum the system is highly Bose degenerate and the quantum field can be treated using a classical field. This description still includes quantum features, hence the formalism is named as c-field methods to avoid the perception that it is a classical treatment.

C-field methods employ a projector operator which creates a cutoff where the occupation of the energy modes becomes approximately one. This means that all the modes below the cutoff can be treated fully quantum mechanically using a classical field representation. The modes above the cutoff are treated semi-classically and represent the thermal cloud. To account for interactions between the condensate and thermal cloud, a stochastic Gross-Pitaevskii equation can be derived by treating the trapped Bose gas as an open system [5, 25, 10]. The thermal cloud is treated as a thermal reservoir which couples to the condensate atoms to include additional damping and noise terms to the Gross-Pitaevskii treatment. The stochastic Gross-Pitaevskii equation has been used to investigate spontaneous vortices in the formation of Bose-Einstein condensates [41], as well as modeling the dynamics of the formation of a rotating Bose-Einstein condensate [11]. However numerical investigations using the stochastic Gross-Pitaevskii equation are currently limited so it is of interest to investigate high temperature Bose-Einstein condensation using this theory.

The very first stochastic Gross-Pitaevskii equation describing such coupling between the thermal cloud and condensate was derived by Stoof [39, 40] using a Keldysh path integral formulation of Quantum Field Theory. This differs from the c-field version as there is no projector operator used, so formally this stochastic Gross-Pitaevskii equation only describes the condensate [36].

### 2.4.2 Vortices in High Temperature Bose-Einstein Condensates

#### Dissipative versus Diffusive Decay

The role of dissipative and diffusive based vortex decay is central to this research. The effect of both on vortex decay is illustrated in figure 1.1. In technical terms, purely dissipative vortex decay can be treated using a damped Gross-Pitaevskii equation. Vortex decay of this form has been studied heavily (see previous research below), while in contrast little is known about the response of a vortex to random fluctuations. To account for fluctuations inducing diffusive vortex decay, a stochastic Gross-Pitaevskii equation including noise must be used. The decay of a single vortex originating at the center of a Bose-Einstein condensate is an

interesting system to test dissipative versus diffusive decay, since a single vortex will have an infinite lifetime at the center of a condensate in the presence of only dissipation [23]. The SGPE will provide a framework to understand the effect both dissipation and diffusion have on single vortex decay.

### Previous Research

There have been a number of theoretical investigations into single vortex dynamics in high temperature Bose-Einstein condensates. Here we outline some recent studies which are relevant to this research.

The stochastic Gross-Pitaevskii equation formed by Stoof [39, 40] has been used to investigate vortex dynamics. Using this theory with a variational ansatz [19], Duine *et al.* [18] found an analytical description of vortex decay in the presence of a thermal cloud. This was generalized to consider a rotating thermal cloud by Bradley and Gardiner [9].

Madarassy and Barenghi [31] investigated vortex motion at finite temperatures involving the interaction with a thermal cloud. They use a phenomenological damping parameter to describe the interaction between the condensate and thermal cloud.

Currently the work by Jackson *et al.* [30] is the most complete numerical investigation of single vortex decay in the presence of a thermal cloud. They use the Zaremba-Nikuni-Griffin (ZNG) formalism [43] where a generalized Gross-Pitaevskii equation is coupled to a Boltzmann equation for the thermal cloud. Their treatment of interactions is not stochastic and they note the fact that stochastic kicks caused by random fluctuations are required to observe vortex decay from the center of a condensate. They create this effect based on the implementation of the ZNG theory in terms of test particles which creates purely statistical fluctuations in the thermal cloud density, which plays the role of noise in their treatment. This is not a complete way of dealing with fluctuations caused by interactions between the vortex and thermal cloud. A full stochastic theory which includes diffusive processes will give a far more complete treatment of vortex dynamics in high temperature Bose-Einstein condensed gases.

In this research we aim to provide the most complete description of vortex dynamics in high temperature Bose-Einstein condensates to date, by using the stochastic Gross-Pitaevskii equation based on c-field methods. As this theory includes diffusive interactions, it will give a more complete view of the role of fluctuations in comparison to dissipation. Such a description has not been seen before as previous studies have essentially focussed on dissipative processes.

# Chapter 3

## C-Field Formalism

*C-field* techniques, utilize the fact that Bose-Einstein condensed systems have significant occupation of many modes of the system. The name is given since when a system has high Bose-degeneracy, the highly occupied modes can be described by a classical field instead of using the full many body quantum field theory. Many of the results in this section are based on a review article by Blakie *et al.* [5], and further details for all these methods can be found there. Here we give a general outline of the formulation of the stochastic Gross-Pitaevskii equation.

### 3.1 Effective Field Theory

The theoretical treatment of many systems of a quantum nature in which quantum statistics are important use second-quantized field theory. Any second-quantized description of Bose fields begins with the second-quantized Hamiltonian describing  $N$  interacting Bosons

$$\hat{H}(t) = \int d^3\mathbf{x} \hat{\Psi}^\dagger(\mathbf{x}, t) H_{\text{sp}} \hat{\Psi}(\mathbf{x}, t) + \frac{1}{2} \int d^3\mathbf{x} \int d^3\mathbf{x}' \hat{\Psi}^\dagger(\mathbf{x}, t) \hat{\Psi}^\dagger(\mathbf{x}', t) U(\mathbf{x} - \mathbf{x}') \hat{\Psi}(\mathbf{x}', t) \hat{\Psi}(\mathbf{x}, t),$$

where the single particle Hamiltonian is of the form

$$H_{\text{sp}} = -\frac{\hbar^2 \nabla^2}{2m} + V_0(\mathbf{x}),$$

and  $V_0(\mathbf{x})$  is the external potential. The second-quantized Bosonic field operator,  $\hat{\Psi}(\mathbf{x}, t)$ , annihilates a particle at position  $\mathbf{x}$  and time  $t$ . These field operators obey the Bosonic commutation relations

$$\left[ \hat{\Psi}(\mathbf{x}, t), \hat{\Psi}(\mathbf{x}', t) \right] = \left[ \hat{\Psi}^\dagger(\mathbf{x}, t), \hat{\Psi}^\dagger(\mathbf{x}', t) \right] = 0 \quad \left[ \hat{\Psi}(\mathbf{x}, t), \hat{\Psi}^\dagger(\mathbf{x}', t) \right] = \delta(\mathbf{x} - \mathbf{x}'). \quad (3.1)$$

The inter-atomic potential,  $U(\mathbf{x} - \mathbf{x}')$ , characterizes two body interactions between Bosons. The magnitude of the interaction potential is set by the effective range parameter  $r_0$  which depends on the relative separation of atoms. Typical temperatures of Bose-Einstein condensation are cold enough (order  $1\mu\text{K}$ ) that the de Broglie wavelength of the atoms is much

larger than their size. Thus length scales of interest in Bose-Einstein condensed systems are larger than the effective range parameter, which means that most details at the atomic level are not important. Short wavelength modes are eliminated by imposing an energy cutoff  $E_{\max}$ , that is, the modes of the system are restricted to a low energy subspace  $\mathbf{L}$ . This cutoff enables the details of small length scales to be ignored, and all scattering between two atoms can be parameterized by the S-wave scattering length. Describing the atomic interactions in this way is known as an *effective field theory*, and the effective Hamiltonian becomes

$$\hat{H}_{\text{eff}} = \int d^3\mathbf{x} \hat{\psi}^\dagger(\mathbf{x}) H_{\text{sp}} \hat{\psi}(\mathbf{x}) + \frac{u}{2} \int d^3\mathbf{x} \hat{\psi}^\dagger(\mathbf{x}) \hat{\psi}^\dagger(\mathbf{x}) \hat{\psi}(\mathbf{x}) \hat{\psi}(\mathbf{x}), \quad (3.2)$$

where the value of the interaction parameter  $u$  is dependent on the S-wave scattering length  $a_s$

$$u = \frac{4\pi a_s \hbar^2}{m}. \quad (3.3)$$

The effective Hamiltonian describes the coarse-grained field operator  $\hat{\psi}(\mathbf{x})$  which only contains modes in  $\mathbf{L}$ , and can be expanded as

$$\hat{\psi}(\mathbf{x}) = \sum_{n \in \mathbf{L}} \hat{a}_n \phi_n(\mathbf{x}), \quad (3.4)$$

where  $\phi_n(\mathbf{x})$  are single-particle eigenstates of  $H_{\text{sp}}$  with energy  $\epsilon_n$

$$\epsilon_n \phi_n(\mathbf{x}) = H_{\text{sp}} \phi_n(\mathbf{x}), \quad (3.5)$$

and the  $\hat{a}_n$  obey the Bose commutation relations

$$[\hat{a}_i, \hat{a}_j] = [\hat{a}_i^\dagger, \hat{a}_j^\dagger] = 0, \quad [\hat{a}_i, \hat{a}_j^\dagger] = \delta_{ij}. \quad (3.6)$$

The effective field theory imposes an energy cutoff so the commutation relations of the  $\hat{\psi}(\mathbf{x})$  are no longer precise delta functions as in (3.1), but become a coarse-grained delta function

$$[\hat{\psi}(\mathbf{x}), \hat{\psi}^\dagger(\mathbf{x}')] = \delta_{\mathbf{L}}(\mathbf{x} - \mathbf{x}'), \quad (3.7)$$

The Heisenberg equation of motion which describes the evolution of the field operator over the included low energy modes in  $\mathbf{L}$  can be found easily using the above commutation relations, and is given by

$$i\hbar \frac{\partial \hat{\psi}(\mathbf{x})}{\partial t} = \int d^3\mathbf{x}' \delta_{\mathbf{L}}(\mathbf{x} - \mathbf{x}') \left\{ H_{\text{sp}} \hat{\psi}(\mathbf{x}') + u \hat{\psi}^\dagger(\mathbf{x}') \hat{\psi}(\mathbf{x}') \hat{\psi}(\mathbf{x}') \right\}. \quad (3.8)$$

Understanding the dynamics of any Bose condensed system requires solving this Heisenberg equation of motion (3.8), however in general this is not an easy task. C-field techniques provide a method to solve (3.8) in different regimes.

## 3.2 Projection into the Classical Field Region

### 3.2.1 Theory of the Projector Operator

The size of the **L** region generated from the effective field theory however is very large and computationally difficult to deal with. By further dividing the **L** region into two regions, classical field methods can be applied to low energy modes which have a high occupation. The system is divided into the following two regions (see figure 3.1):

- (i) The *condensate band* (**C**) consisting of low energy modes with significant occupation. This region contains highly occupied modes which will be treated using a classical field. For temperatures below the transition, this contains the condensate and low energy excitations.
- (ii) The *non-condensate band* (**NC**) which contains all modes in **L** which are not in the **C** region. These modes are weakly occupied, and for many systems are essentially thermalized.

The single particle energy  $\epsilon_{\text{cut}}$  defines the condensate and non-condensate bands by requiring that the **C** region corresponds to energies  $\epsilon \leq \epsilon_{\text{cut}}$ , and that the **NC** region corresponds to energies  $\epsilon_{\text{cut}} < \epsilon < E_{\text{max}}$ . The field operator can be restricted to a certain region by using

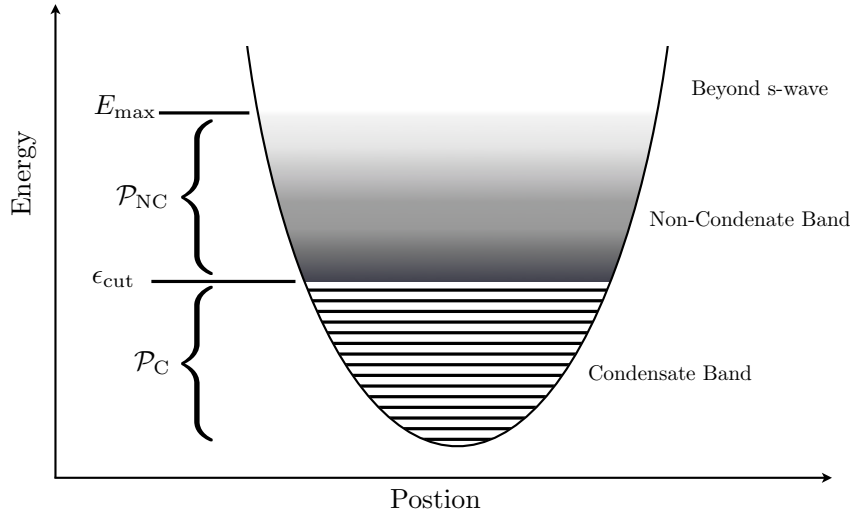


Figure 3.1: A schematic showing the condensate band, non-condensate band, and states eliminated to give the effective field theory. In the stochastic Gross-Pitaevskii equation, the condensate band is treated quantum mechanically in a classical field approximation. The non-condensate band is treated semi-classically, and is most simply described as a grand canonical reservoir.



orthogonal projector operators, which are defined for the two regions by

$$\mathcal{P}_{\mathbf{C}} \{F(\mathbf{x})\} \equiv \sum_{n \in \mathbf{C}} \phi_n(\mathbf{x}) \int d^3 \mathbf{x}' \phi_n^*(\mathbf{x}') F(\mathbf{x}'), \quad (3.9)$$

$$\mathcal{P}_{\mathbf{NC}} \{F(\mathbf{x})\} \equiv \sum_{n \in \mathbf{NC}} \phi_n(\mathbf{x}) \int d^3 \mathbf{x}' \phi_n^*(\mathbf{x}') F(\mathbf{x}'), \quad (3.10)$$

where  $\mathbf{C} = \{n : \epsilon_n \leq \epsilon_{\text{cut}}\}$  and  $\mathbf{NC} = \{n : \epsilon_{\text{cut}} < \epsilon_n \leq E_{\text{max}}\}$ , so  $\mathbf{L} = \mathbf{C} + \mathbf{NC}$  and  $\mathcal{P}_{\mathbf{C}} \mathcal{P}_{\mathbf{NC}} = 0$ .

The quantum field operators for each region can be defined by applying the projector operators on the total field operator  $\hat{\psi}$

$$\hat{\psi}_{\mathbf{C}}(\mathbf{x}) \equiv \mathcal{P}_{\mathbf{C}} \{\hat{\psi}(\mathbf{x})\} = \sum_{n \in \mathbf{C}} \hat{a}_n \phi_n(\mathbf{x}), \quad (3.11)$$

$$\hat{\psi}_{\mathbf{NC}}(\mathbf{x}) \equiv \mathcal{P}_{\mathbf{NC}} \{\hat{\psi}(\mathbf{x})\} = \sum_{n \in \mathbf{NC}} \hat{a}_n \phi_n(\mathbf{x}), \quad (3.12)$$

so the total field operator can be written as a sum corresponding to the field operator in both the condensate and non-condensate bands

$$\hat{\psi}(\mathbf{x}) = \hat{\psi}_{\mathbf{C}}(\mathbf{x}) + \hat{\psi}_{\mathbf{NC}}(\mathbf{x}). \quad (3.13)$$

An important consequence of the projection is that the commutator of the condensate band operator is not a pure Dirac-delta function, but is of the form

$$[\hat{\psi}_{\mathbf{C}}(\mathbf{x}), \hat{\psi}_{\mathbf{C}}^\dagger(\mathbf{x}')] = \delta_{\mathbf{C}}(\mathbf{x}, \mathbf{x}') \quad (3.14)$$

where  $\delta_{\mathbf{C}}(\mathbf{x}, \mathbf{x}')$  is known formally as the kernel of the condensate projector,  $\mathcal{P}_{\mathbf{C}}$ ,

$$\delta_{\mathbf{C}}(\mathbf{x}, \mathbf{x}') \equiv \sum_{n \in \mathbf{C}} \phi_n(\mathbf{x}) \phi_n^*(\mathbf{x}'). \quad (3.15)$$

Although the commutator (3.14) is not a pure Dirac-delta function, it acts as one on any function in the projected region. So for any function in the condensate band

$$\int d^3 \mathbf{x}' \delta_{\mathbf{C}}(\mathbf{x}, \mathbf{x}') \psi_{\mathbf{C}}(\mathbf{x}') = \psi_{\mathbf{C}}(\mathbf{x}) \quad (3.16)$$

### 3.2.2 Full Hamiltonian

Using the field operator decomposition (3.13), the effective Hamiltonian (3.2) can be written in terms of  $\hat{\psi}_{\mathbf{C}}$  and  $\hat{\psi}_{\mathbf{NC}}$  in the form

$$\hat{H}_{\text{eff}} = \hat{H}_{\mathbf{C}} + \hat{H}_{\mathbf{NC}} + \hat{H}_{I,\mathbf{C}} \quad (3.17)$$

where  $\hat{H}_{\mathbf{C}}$  involves only the condensate band field operators,  $\hat{H}_{\mathbf{NC}}$  involves only non-condensate band field operators and

$$\hat{H}_{I,\mathbf{C}} = \hat{H}_{I,\mathbf{C}}^{(1)} + \hat{H}_{I,\mathbf{C}}^{(2)} + \hat{H}_{I,\mathbf{C}}^{(3)} \quad (3.18)$$

represents atomic interaction terms involving one, two or three condensate band operators. The terms take the form of

$$\hat{H}_C = \int d^3\mathbf{x} \hat{\psi}_C^\dagger(\mathbf{x}) H_{\text{sp}} \hat{\psi}_C(\mathbf{x}) + \frac{u}{2} \int d^3\mathbf{x} \hat{\psi}_C^\dagger(\mathbf{x}) \hat{\psi}_C^\dagger(\mathbf{x}) \hat{\psi}_C(\mathbf{x}) \hat{\psi}_C(\mathbf{x}) \quad (3.19)$$

$$\hat{H}_{NC} = \int d^3\mathbf{x} \hat{\psi}_{NC}^\dagger(\mathbf{x}) H_{\text{sp}} \hat{\psi}_{NC}(\mathbf{x}) + \frac{u}{2} \int d^3\mathbf{x} \hat{\psi}_{NC}^\dagger(\mathbf{x}) \hat{\psi}_{NC}^\dagger(\mathbf{x}) \hat{\psi}_{NC}(\mathbf{x}) \hat{\psi}_{NC}(\mathbf{x}) \quad (3.20)$$

$$\hat{H}_{I,C}^{(1)} = u \int d^3\mathbf{x} \hat{\psi}_{NC}^\dagger(\mathbf{x}) \hat{\psi}_{NC}^\dagger(\mathbf{x}) \hat{\psi}_{NC}(\mathbf{x}) \hat{\psi}_C(\mathbf{x}) + \text{h.c.} \quad (3.21)$$

$$\begin{aligned} \hat{H}_{I,C}^{(2)} &= u \int d^3\mathbf{x} \hat{\psi}_{NC}^\dagger(\mathbf{x}) \hat{\psi}_{NC}(\mathbf{x}) \hat{\psi}_C^\dagger(\mathbf{x}) \hat{\psi}_C(\mathbf{x}) + \text{h.c.} \\ &+ \frac{u}{2} \int d^3\mathbf{x} \hat{\psi}_{NC}^\dagger(\mathbf{x}) \hat{\psi}_{NC}^\dagger(\mathbf{x}) \hat{\psi}_C(\mathbf{x}) \hat{\psi}_C(\mathbf{x}) + \text{h.c.} \end{aligned} \quad (3.22)$$

$$\hat{H}_{I,C}^{(3)} = u \int d^3\mathbf{x} \hat{\psi}_C^\dagger(\mathbf{x}) \hat{\psi}_C^\dagger(\mathbf{x}) \hat{\psi}_C(\mathbf{x}) \hat{\psi}_{NC}(\mathbf{x}) + \text{h.c.} \quad (3.23)$$

where h.c. denotes the Hermitian-conjugate. Terms arising from the single particle Hamiltonian involving one  $\hat{\psi}_C$  and one  $\hat{\psi}_{NC}$  have no contribution as the non-condensate band operators have no mean field.

### 3.2.3 C-Field Methods

There are three c-field methods which differ in the way they treat the different interaction Hamiltonians, which contain field operators of both the condensate and non-condensate band. These three techniques are

(i) **Projected Gross-Pitaevskii Equation (PGPE)**

The PGPE is simply the Gross-Pitaevskii equation where evolution is restricted to the condensate band. In this case all cross terms involving the the interaction Hamiltonians are neglected, so the PGPE does not account for any coupling between the condensate and non-condensate band. The PGPE thus treats the condensate band as a microcanonical system of fixed number and energy.

(ii) **Stochastic Gross-Pitaevskii Equation (SGPE)**

The SGPE retains all interaction terms, hence it accounts for coupling between the condensate and non-condensate bands. Such scattering processes are implemented in theory by finding a stochastic differential equation with dissipative and stochastic noise terms. Since SGPE deals with the interaction between the two bands, occupation of the non-condensate band can be accounted for. Hence SGPE is a high temperature theory which is suitable for temperatures much higher than the single particle energy,  $\hbar\omega \ll k_B T$ , where there is a significant thermal component.

(iii) **Truncated Wigner Projected Gross-Pitaevskii Equation (TWPGPE)**

The TWPGPE is of use when there are modes with low occupation in the condensate band. The population of the non-condensate band is negligible meaning the cross terms in the interacting Hamiltonians can be dropped. To model this system containing

modes of low occupation quantum mechanically, additional noise must be added to account for quantum fluctuations. These quantum fluctuations can be approximated by sampling the initial Wigner distribution, and leads to the ability to describe non-equilibrium dynamics of Bose-Einstein condensation at low temperatures  $T \ll T_c$ . Such a system with low occupation of modes is not directly relevant to high temperature systems of interest here, but the truncated Wigner theory is central to the SGPE.

In terms of describing high temperature Bose-Einstein condensation, where  $\hbar\omega \ll k_B T$ , the SGPE will give the most complete account of the system as it treats scattering processes with thermally occupied modes. Thus the SGPE will be the primary tool in the investigation of vortex dynamics in high temperature Bose-Einstein condensation. Since the SGPE is based on the PGPE, and on the truncated Wigner approximation, it is necessary to consider these in the formulation of SGPE theory, even though in practice these methods will not be directly used.

## 3.3 Wigner Formalism

### 3.3.1 Overview of Phase-Space Methods

In all c-field methods, the energy cutoff  $\epsilon_{\text{cut}}$  is chosen so all modes in the condensate band have significant occupation. In this case the system is highly quantum degenerate and the full quantum description can be treated by a classical description. Although this Bose degenerate system is being represented by a classical field, the quantum mechanical nature of the system is retained through the interpretation of the classical variables. This is done by mapping the evolution of the quantum density operator to a classical quasi-probability function known as the Wigner function. The key to phase space methods is that the equation of motion for the quasi-probability distribution can be mapped to an equivalent stochastic differential equation, which is much easier to solve than the quantum problem with a large Hilbert space. The background behind phase space methods and the Wigner representation of the quantum field has been discussed in detail by Gardiner and Zoller in their book [28]. In this section, we detail the results and methods which are important to the formulation of the SGPE.

### 3.3.2 Coherent States

The limit of  $\hbar \rightarrow 0$  corresponds to the approach of the transition from a quantum to classical description of the dynamics of a system. However in some systems, the approach to this limit is not consistent with classical motion. By finding states of minimum uncertainty,  $|\alpha\rangle$ , one will have found states which display behavior which is the closest to classical of any quantum state. These states satisfy

$$a|\alpha\rangle = \alpha|\alpha\rangle, \quad (3.24)$$

where  $a$  is the annihilation operator,  $\alpha$  is a complex number, and the states  $|\alpha\rangle$  are known as coherent states. Coherent states are one of the most important tools of studying Bose gases, and are used throughout the Wigner representation of the quantum field.

### 3.3.3 Wigner Representation of a Single Quantum Mode

If a system has a state vector  $|\psi, t\rangle$ , then the density operator is defined by the outer product

$$\rho(t) = |\psi, t\rangle\langle\psi, t|. \quad (3.25)$$

Phase space methods rely on expressing the density operator in terms of a c-number function of a coherent state variable  $\alpha$ . The Wigner representation makes such a connection through the Wigner function, which expresses the density operator on a basis of coherent states. The Wigner function  $W(\alpha, \alpha^*)$  was introduced by Wigner in 1932 [42], and is defined as the Fourier transform of the symmetrically ordered quantum characteristic function

$$W(\alpha, \alpha^*) = \frac{1}{\pi^2} \int d^2\lambda \exp[-\lambda\alpha^* + \lambda^*\alpha] \chi(\lambda, \lambda^*), \quad (3.26)$$

where the symmetrically ordered quantum characteristic function is given by

$$\chi(\lambda, \lambda^*) = \text{tr} \left\{ \rho \exp[\lambda a^\dagger - \lambda^* a] \right\}. \quad (3.27)$$

An important fact about the Wigner function is that it exists for any density operator [28], so it is always possible to get a c-number function of  $\alpha$  if a density operator is defined. The key to phase space methods is based on the ability to map the action of a quantum operator on a density operator to the action of a differential operator on the Wigner function. It is well known that the following operator correspondences exist for the actions of the creation and destruction operators on the density operator [28]

$$a\rho \longleftrightarrow \left( \alpha + \frac{1}{2} \frac{\partial}{\partial \alpha^*} \right) W(\alpha, \alpha^*) \quad (3.28)$$

$$a^\dagger \rho \longleftrightarrow \left( \alpha^* - \frac{1}{2} \frac{\partial}{\partial \alpha} \right) W(\alpha, \alpha^*) \quad (3.29)$$

$$\rho a \longleftrightarrow \left( \alpha - \frac{1}{2} \frac{\partial}{\partial \alpha^*} \right) W(\alpha, \alpha^*) \quad (3.30)$$

$$\rho a^\dagger \longleftrightarrow \left( \alpha^* + \frac{1}{2} \frac{\partial}{\partial \alpha} \right) W(\alpha, \alpha^*) \quad (3.31)$$

These operator correspondences are a crucial aspect of phase space methods in that they can make the equations of motion of the quantum system much simpler, creating an easier path to a solution.

### 3.3.4 Wigner Representation of the Quantum Field

The properties of the Wigner function in the single mode case extend naturally to the full multimode system needed to describe our system. For a system of  $M$  modes in the condensate band, the multimode Wigner function is given by [5]

$$W_{\mathbf{C}}(\boldsymbol{\alpha}, \boldsymbol{\alpha}^*) = \int \frac{d^2\boldsymbol{\lambda}}{\pi^{2M}} \exp(\boldsymbol{\lambda}^\dagger \boldsymbol{\alpha} - \boldsymbol{\alpha}^\dagger \boldsymbol{\lambda}) \chi(\boldsymbol{\lambda}, \boldsymbol{\lambda}^*), \quad (3.32)$$

where  $\boldsymbol{\alpha}$  is defined as the vector of mode amplitudes  $\boldsymbol{\alpha} = [\alpha_0, \alpha_1, \dots, \alpha_{M-1}]$ ,  $\chi(\boldsymbol{\lambda}, \boldsymbol{\lambda}^*)$  is the symmetric quantum characteristic function for the condensate band density operator  $\rho_{\mathbf{C}}$ , and where

$$\int d^2\boldsymbol{\alpha} \equiv \prod_{n \in \mathbf{C}} \int d^2\alpha_n. \quad (3.33)$$

The classical field,  $\psi_{\mathbf{C}}$ , can be expanded over single-particle energy states using the mode amplitudes

$$\psi_{\mathbf{C}}(\mathbf{x}) = \sum_{n \in \mathbf{C}} \alpha_n \phi_n(\mathbf{x}), \quad (3.34)$$

which is the classical field function representing the condensate band. An important result is found by looking at the classical field average which can be found using the fact that moments of the Wigner distribution give symmetrically ordered operator averages. The field density average is given by

$$\begin{aligned} \int d^2\boldsymbol{\alpha} |\psi_{\mathbf{C}}(\mathbf{x})|^2 W_{\mathbf{C}}(\boldsymbol{\alpha}, \boldsymbol{\alpha}^*) &= \left\langle \frac{\hat{\Psi}_{\mathbf{C}}^\dagger(\mathbf{x}) \hat{\Psi}_{\mathbf{C}}(\mathbf{x}) + \hat{\Psi}_{\mathbf{C}}(\mathbf{x}) \hat{\Psi}_{\mathbf{C}}^\dagger(\mathbf{x})}{2} \right\rangle, \\ &= \left\langle \hat{\Psi}_{\mathbf{C}}^\dagger(\mathbf{x}) \hat{\Psi}_{\mathbf{C}}(\mathbf{x}) \right\rangle + \frac{\delta_{\mathbf{C}}(\mathbf{x}, \mathbf{x})}{2}. \end{aligned} \quad (3.35)$$

This is an important result as there is the presence of vacuum noise in the commutator term  $\delta_{\mathbf{C}}(\mathbf{x}, \mathbf{x})$  (from (3.14)), which accounts for half a quantum per mode of noise. This shows that quantum effects are still present in the Wigner representation.

As in the single mode case, operator correspondences between the density operator  $\rho_{\mathbf{C}}$  and the Wigner function can be derived. The multimode calculations can be simplified by defining the *projected functional derivative operators*

$$\frac{\bar{\delta}}{\delta \psi_{\mathbf{C}}(\mathbf{x})} \equiv \sum_{n \in \mathbf{C}} \phi_n^*(\mathbf{x}) \frac{\partial}{\partial \alpha_n}, \quad (3.36)$$

$$\frac{\bar{\delta}}{\delta \psi_{\mathbf{C}}^*(\mathbf{x})} \equiv \sum_{n \in \mathbf{C}} \phi_n(\mathbf{x}) \frac{\partial}{\partial \alpha_n^*}. \quad (3.37)$$

Using these projected functional derivatives, the operator correspondences between  $\rho_{\mathbf{C}}$  and the Wigner function can be easily found

$$\hat{\psi}_{\mathbf{C}}(\mathbf{x}) \rho_{\mathbf{C}} \longleftrightarrow \left( \psi_{\mathbf{C}}(\mathbf{x}) + \frac{1}{2} \frac{\bar{\delta}}{\delta \psi_{\mathbf{C}}^*(\mathbf{x})} \right) W_{\mathbf{C}}, \quad (3.38)$$

$$\hat{\psi}_{\mathbf{C}}^{\dagger}(\mathbf{x})\rho_{\mathbf{C}} \longleftrightarrow \left( \psi_{\mathbf{C}}^*(\mathbf{x}) - \frac{1}{2} \frac{\bar{\delta}}{\bar{\delta}\psi_{\mathbf{C}}(\mathbf{x})} \right) W_{\mathbf{C}}, \quad (3.39)$$

$$\rho_{\mathbf{C}}\hat{\psi}_{\mathbf{C}}(\mathbf{x}) \longleftrightarrow \left( \psi_{\mathbf{C}}(\mathbf{x}) - \frac{1}{2} \frac{\bar{\delta}}{\bar{\delta}\psi_{\mathbf{C}}^*(\mathbf{x})} \right) W_{\mathbf{C}}, \quad (3.40)$$

$$\rho_{\mathbf{C}}\hat{\psi}_{\mathbf{C}}^{\dagger}(\mathbf{x}) \longleftrightarrow \left( \psi_{\mathbf{C}}^*(\mathbf{x}) + \frac{1}{2} \frac{\bar{\delta}}{\bar{\delta}\psi_{\mathbf{C}}(\mathbf{x})} \right) W_{\mathbf{C}}. \quad (3.41)$$

These operator correspondences are used to map the equation of motion of  $\rho_{\mathbf{C}}$  to an equivalent equation of motion for the Wigner function  $W_{\mathbf{C}}$ .

### 3.3.5 The Truncated Wigner Approximation

The evolution of the density operator in the condensate band is given by von Neumann's equation

$$i\hbar \frac{\partial \hat{\rho}_{\mathbf{C}}(t)}{\partial t} = [\hat{H}_{\mathbf{C}}, \hat{\rho}_{\mathbf{C}}(t)], \quad (3.42)$$

where we consider no interactions between the condensate and non-condensate band. This equation is in general not trivial to solve, so the operator correspondences are used to make a transformation to an evolution equation of the Wigner function. Using the operator correspondences for the multimode Wigner function (3.38 - 3.41) leads to the evolution equation

$$\begin{aligned} \left. \frac{\partial W_{\mathbf{C}}}{\partial t} \right|_{\hat{H}_{\mathbf{C}}} &= \int d^3\mathbf{x} \left\{ \frac{i u}{4\hbar} \frac{\bar{\delta}}{\bar{\delta}\psi_{\mathbf{C}}(\mathbf{x})\bar{\delta}\psi_{\mathbf{C}}^*(\mathbf{x})} \psi_{\mathbf{C}}^*(\mathbf{x}) \frac{\bar{\delta}}{\bar{\delta}\psi_{\mathbf{C}}^*(\mathbf{x})} + \text{h.c.} \right. \\ &\quad \left. \frac{i}{\hbar} \frac{\bar{\delta}}{\bar{\delta}\psi_{\mathbf{C}}(\mathbf{x})} (H_{\text{sp}} + u[|\psi_{\mathbf{C}}(\mathbf{x})|^2 - \delta_{\mathbf{C}}(\mathbf{x}, \mathbf{x})]) \psi_{\mathbf{C}}(\mathbf{x}) + \text{h.c.} \right\} W_{\mathbf{C}}. \end{aligned} \quad (3.43)$$

This equation represents the time evolution of the classical field  $\psi_{\mathbf{C}}(\mathbf{x})$ , and is very difficult to solve due to the third-order derivatives. However, this evolution equation becomes manageable if these third-order derivatives are neglected. This approximation is known as the *truncated Wigner approximation* and is often made in c-field methods. Making the truncated Wigner approximation gives

$$\left. \frac{\partial W_{\mathbf{C}}}{\partial t} \right|_{\hat{H}_{\mathbf{C}}} = \int d^3\mathbf{x} \left\{ \frac{i}{\hbar} \frac{\bar{\delta}}{\bar{\delta}\psi_{\mathbf{C}}(\mathbf{x})} (H_{\text{sp}} + u[|\psi_{\mathbf{C}}(\mathbf{x})|^2 - \delta_{\mathbf{C}}(\mathbf{x}, \mathbf{x})]) \psi_{\mathbf{C}}(\mathbf{x}) + \text{h.c.} \right\} W_{\mathbf{C}} \quad (3.44)$$

which takes the form of a Fokker-Planck equation with drift due to the presence of the first order derivative, but with no diffusion terms due to the absence of second order derivatives. Making the truncated Wigner approximation is valid in many circumstances [5]. In terms of c-field theory, the approximation is valid when the modes in question have significant population. Hence c-field methods require macroscopic occupation in the condensate band modes so that the truncated Wigner approximation can be made.

A general property of Fokker-Planck equations is that they can be mapped to an equivalent stochastic partial differential equation if the diffusion matrix is positive semidefinite [24]. Such a mapping is not possible for the full equation representing the Wigner function evolution (3.43) due to the third order derivatives. The truncated Wigner approximation leads to an evolution equation which corresponds to a stochastic partial differential equation which is comparatively much easier to solve. Making this mapping gives the following differential equation, known as the TWPGPE

$$i\hbar \frac{\partial \psi_{\mathbf{C}}(\mathbf{x})}{\partial t} = \mathcal{P}_{\mathbf{C}} \left\{ \left( H_{\text{sp}} + u[|\psi_{\mathbf{C}}(\mathbf{x})|^2 - \delta_{\mathbf{C}}(\mathbf{x}, \mathbf{x}')] \right) \psi_{\mathbf{C}}(\mathbf{x}) \right\}. \quad (3.45)$$

This differential equation is not explicitly stochastic, but noise is introduced by sampling the Wigner function which introduces a random element corresponding to occupation of half a quantum per mode. The TWPGPE (3.45) on its own in this form is not directly applicable to the high temperature regime, but the method behind its derivation is important in terms of how the SGPE is found.

### 3.4 The Projected Gross-Pitaevskii Equation

The PGPE is derived simply by applying the projector operator (3.11) to the Heisenberg equation of motion (3.8) [16]. As stated, the PGPE neglects all coupling between the condensate and non-condensate bands, so the resulting Heisenberg equation of motion just includes the Hamiltonian based on the condensate band field operators (3.19). Also as the PGPE is a c-field theory, the mode occupation of the condensate band must be macroscopic. The result is the PGPE

$$i\hbar \frac{\partial \psi_{\mathbf{C}}(\mathbf{x})}{\partial t} = \mathcal{P}_{\mathbf{C}} \left\{ (H_{\text{sp}} + u|\psi_{\mathbf{C}}(\mathbf{x})|^2) \psi_{\mathbf{C}}(\mathbf{x}) \right\}. \quad (3.46)$$

### 3.5 The Stochastic Gross-Pitaevskii Equation

The SGPE formulation used in this work accounts for interactions between the two bands by treating the non-condensate band as fully thermalized, that is, a grand-canonical reservoir at a specific temperature and chemical potential. As interactions between the condensate and non condensate bands are not neglected, all terms from the effective Hamiltonian (3.17) are included in von Neumann's equation describing the evolution of the density operator. The SGPE can be thought of as an extension of the PGPE to include the interactions between the two bands, and these interactions generate damping and stochastic noise terms in addition to the PGPE. The full derivation of the master equation arising from the effective Hamiltonian (3.17), and subsequent formulation of the stochastic differential equations leading to the SGPE has been well documented [25, 10]. The full details of these calculations are omitted due to the complexity of the derivations. In this section we outline the key details leading to the formulation of the SGPE.

### 3.5.1 The Master Equation

The equation of motion for the density operator for the full system including both the condensate and non-condensate bands is given by the von Neumann equation

$$\dot{\rho} = -\frac{i}{\hbar} \left[ \hat{H}_C + \hat{H}_{NC} + \hat{H}_{I,C}, \rho \right]. \quad (3.47)$$

The standard procedure for using phase-space methods for open systems is based on finding a master equation for the reduced system, that is the condensate density operator, by eliminating the reservoir degrees of freedom [28, 26, 27, 29]. This is done by defining the condensate band density operator as the trace of  $\rho$  over the non-condensate band degrees of freedom

$$\rho_C \equiv \text{tr}_{NC}\{\rho\}. \quad (3.48)$$

Since the full effective Hamiltonian (3.17) must be used, a number of different terms arise based on interactions between the condensate and non-condensate band. Accounting for all interactions using the condensate band density operator leads to the full master equation for the reduced system

$$\dot{\rho}_C = \dot{\rho}_C|_{\text{Ham}} \quad (3.49a)$$

$$+ \dot{\rho}_C|_{\text{growth}} \quad (3.49b)$$

$$+ \dot{\rho}_C|_{\text{scatt}}. \quad (3.49c)$$

The first term  $\dot{\rho}_C|_{\text{Ham}}$  corresponds to the term from von Neumann's equation originating from the Hamiltonian  $H_C$  (3.19) involving just the condensate band field operator. This term is exactly the same as (3.42) used in deriving the TWPGPE. The other two terms,  $\dot{\rho}_C|_{\text{growth}}$  and  $\dot{\rho}_C|_{\text{scatt}}$ , arise from the interaction Hamiltonian (3.18). These terms have the name growth and scattering due to the nature of the interaction processes which are described by the different terms which emerge due to the interaction Hamiltonian.

### 3.5.2 The Stochastic Gross-Pitaevskii Equation

The full master equation (3.49) is mapped to an evolution equation for the Wigner function using the operator correspondences (3.38 - 3.41) as in section 3.3.5 where the TWPGPE was derived. Similarly, this leads to a partial differential equation containing third order derivatives. and the truncated Wigner approximation is made to give a Fokker-Planck equation. The mapping of the Fokker-Planck equation to a stochastic differential equation gives the full SGPE

$$(S)d\psi_C(\mathbf{x}, t) = \mathcal{P}_C \left\{ -\frac{i}{\hbar} \left( H_{\text{sp}} + u|\psi_C(\mathbf{x}, t)|^2 \right) \psi_C(\mathbf{x}, t) dt \right. \quad (3.50a)$$

$$+ \frac{G(\mathbf{x})}{k_B T} \left[ \mu - \left( H_{\text{sp}} + u|\psi_C(\mathbf{x}, t)|^2 \right) \right] \psi_C(\mathbf{x}, t) dt + dW_G(\mathbf{x}, t) \quad (3.50b)$$

$$\left. + \int d^3\mathbf{x}' M(\mathbf{x} - \mathbf{x}') \frac{i\hbar \nabla \cdot \mathbf{j}_C(\mathbf{x}')}{k_B T} \psi_C(\mathbf{x}, t) dt + i\psi_C(\mathbf{x}) dW_M(\mathbf{x}, t) \right\} \quad (3.50c)$$



where the  $(S)$  indicates that the stochastic differential equation is given in Stratonovich form. The first line of the SGPE is simply the PGPE (3.46) where there is no representation of coupling between the condensate and non-condensate band.

The effect of coupling from the interaction Hamiltonians is introduced into the SGPE through the growth and scattering terms in the master equation (3.49b, 3.49c), and relate to the second and third lines of the SGPE respectively.

### 3.5.3 Growth and Scattering Processes

Including interactions between the condensate and non-condensate band leads to dissipative and noise terms which can be seen to originate physically from growth and scattering processes (see figure 3.2). Here we give a brief description of these processes.

#### Growth Processes

The second line of the SGPE (3.50b) is responsible for growth in the condensate band by scattering of two thermal atoms in the non-condensate band. The  $\mu$  and  $T$  which appear correspond to the temperature and chemical potential of the thermal reservoir containing atoms in the non-condensate band. The growth term  $G(\mathbf{x})$  represents the collision rate of particles in the non-condensate band and acts as a damping term in the equation of motion. The noise associated with the growth process is  $dW_G(\mathbf{x}', t)$ , defined by

$$\langle dW_G^*(\mathbf{x}, t)dW_G(\mathbf{x}', t) \rangle = 2G(\mathbf{x})\delta_C(\mathbf{x}, \mathbf{x}')dt, \quad (3.51)$$

$$\langle dW_G(\mathbf{x}, t)dW_G(\mathbf{x}', t) \rangle = \langle dW_G^*(\mathbf{x}, t)dW_G^*(\mathbf{x}', t) \rangle = 0, \quad (3.52)$$

where the noise is complex and additive.

The growth rate can be calculated for the non-condensate band in thermal equilibrium at chemical potential  $\mu$  and temperature  $T$ , and takes the form [11]

$$G(\mathbf{x}) = \gamma, \quad (3.53)$$

where

$$\gamma = \gamma_0 \left\{ [\ln(1 - e^{\beta(\mu - \epsilon_{\text{cut}})})]^2 + e^{2\beta(\mu - \epsilon_{\text{cut}})} \sum_{r=1}^{\infty} e^{r\beta(\mu - 2\epsilon_{\text{cut}})} \left( \Phi[e^{\beta(\mu - \epsilon_{\text{cut}})}, 1, r + 1] \right)^2 \right\}, \quad (3.54)$$

where the rate constant is  $\gamma_0 = 4m(a_s k_B T)^2 / \pi \hbar^3$ , and  $\Phi[x, y, z]$  is the Lerch transcendent defined by

$$\Phi[z, s, a] = \sum_{k=0}^{\infty} \frac{z^k}{(a+k)^s}. \quad (3.55)$$

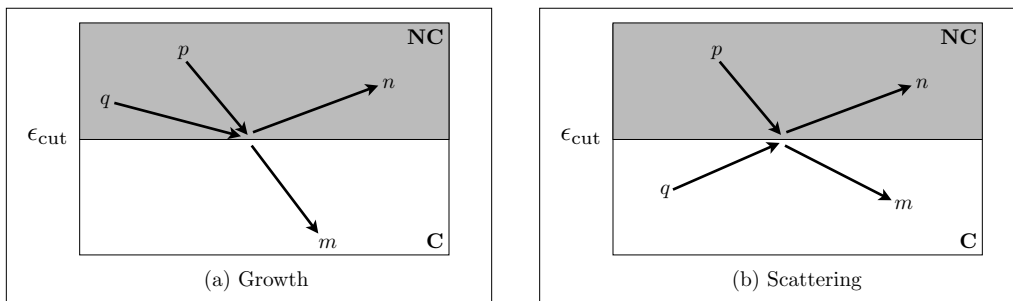


Figure 3.2: Growth and scattering processes caused by interactions between the condensate and non-condensate bands. The growth process (a) occurs when two non-condensate band atoms collide, the energy is transferred to one of the atoms, while the other enters the condensate band. The scattering process (b) occurs when a condensate and non-condensate atom collide, leaving no change in either band's population.

### Scattering Processes

The third line of the SGPE (3.50c) is responsible for scattering processes which conserve the number of atoms in both the condensate and non-condensate band, while providing a mechanism for energy transfer between the two bands. This couples to the divergence of the condensate band current by

$$\mathbf{j}_{\mathbf{C}}(\mathbf{x}) \equiv \frac{i\hbar}{2m} \left\{ [\nabla\psi_{\mathbf{C}}^*(\mathbf{x})]\psi_{\mathbf{C}}(\mathbf{x}) - \psi_{\mathbf{C}}^*(\mathbf{x})\nabla\psi_{\mathbf{C}}(\mathbf{x}) \right\}. \quad (3.56)$$

In the scattering process, the noise is real and defined by

$$\langle dW_{\mathbf{M}}(\mathbf{x}, t)dW_{\mathbf{M}}(\mathbf{x}', t) \rangle = 2M(\mathbf{x} - \mathbf{x}')dt, \quad (3.57)$$

where  $M(\mathbf{x} - \mathbf{x}')$  is the scattering rate function.

#### 3.5.4 Simple Growth SGPE

The scattering process term from the full SGPE (3.50c) involves the collision of a condensate and non-condensate atom resulting in no change in the population of the condensate band. This is in contrast to the growth term (3.50b) which describes the dominant collision process resulting in Bose-Einstein condensation. This means it is reasonable to expect that the scattering term will be less important than the growth term in describing the condensate dynamics. It seems reasonable physically to neglect the scattering term, but it is also an appealing approximation as the scattering term is very difficult to implement numerically [5]. Neglecting the scattering term leads to the simple growth SGPE

$$\begin{aligned}
(S)d\psi_{\mathbf{C}}(\mathbf{x}, t) &= \mathcal{P}_{\mathbf{C}} \left\{ -\frac{i}{\hbar} \left( H_{\text{sp}} + u|\psi_{\mathbf{C}}(\mathbf{x}, t)|^2 \right) \psi_{\mathbf{C}}(\mathbf{x}, t) dt \right. \\
&\quad \left. + \frac{\gamma}{k_{\text{B}}T} \left[ \mu - \left( H_{\text{sp}} + u|\psi_{\mathbf{C}}(\mathbf{x}, t)|^2 \right) \right] \psi_{\mathbf{C}}(\mathbf{x}, t) dt + dW_{\gamma}(\mathbf{x}, t) \right\}, \quad (3.58)
\end{aligned}$$

where

$$\langle dW_{\gamma}^*(\mathbf{x}, t) dW_{\gamma}(\mathbf{x}', t) \rangle = 2\gamma \delta_{\mathbf{C}}(\mathbf{x}, \mathbf{x}') dt, \quad (3.59)$$

The noise term in the simple growth SGPE is additive, so the numerical implementation of this equation is only slightly more complicated than the PGPE.

The simple growth SGPE (3.58) with  $\gamma$  found by (3.54), is used in this work to simulate vortex dynamics in high temperature Bose-Einstein condensates. Numerical methods for its simulation have been developed [4, 6], and we use an adaptive Runge-Kutta method in the interaction picture [8, 15] to solve (3.58) numerically. In the next section, we describe an accurate and efficient method for choosing SGPE parameters for a wide range of temperatures. The combination of using this calculated growth rate, and an accurate choice of SGPE parameters, means this is the most complete first principles treatment of damping in the SGPE that has been used in actual calculations.

# Chapter 4

## SGPE Parameters

### 4.1 Overview

The SGPE is a grand-canonical theory so the entire system is characterized by the reservoir temperature  $T$  and chemical potential  $\mu$ , which are the control parameters of the theory. The appearance of temperature as a parameter is appealing as this means the temperature of the system can be directly controlled. This is in contrast to the other c-field methods which are microcanonical theories, where the energy and number of atoms are fixed. To investigate high temperature Bose-Einstein condensation using the SGPE, it is desirable to run simulations sweeping through different temperatures relative to the same critical temperature  $T_c$ . However as  $T_c$  is a function of the total number of atoms, simply stepping through a range of temperature parameters while holding  $\mu$  fixed will not give temperatures relative to the same  $T_c$ , as the total atom number will increase significantly. Thus the choice of  $\mu(T)$  is critical to ensure that the total number of atoms in the system is held constant, so the range of temperatures used are relative to the same  $T_c$ .

As well as the parameter  $\mu(T)$ , the energy cutoff  $\epsilon_{\text{cut}}(T)$  needs to be specified. The SGPE is a c-field theory so the mode occupation at the cutoff,  $n_{\text{cut}}$ , needs to be appreciable (between 1 and 10 usually). The energy cutoff must be carefully chosen so that this requirement is met. Control over the parameters is essential to be able to study systems of fixed atom number, however finding  $\mu$  and  $\epsilon_{\text{cut}}$  as a function of temperature exactly so that the total number of atoms remains constant is not trivial. To date this has been done by adjusting  $\mu$  and  $\epsilon_{\text{cut}}$  by trial and error, typically requiring of order 10 simulations and many hours of computing time to obtain the appropriate parameters for a single temperature. By treating interactions between the atoms in the Bose-Einstein condensate and surrounding thermal atoms using a Hartree-Fock approximation, we derive a method in which relatively simple calculations can be made to give an estimate of the appropriate SGPE parameters. The details of this method are presented in this section, along with results of SGPE simulations showing that the calculations lead to a physically consistent choice of parameters.

## 4.2 Methods

The theory behind the calculations to estimate the SGPE parameters is based on methods used by Blakie and Davis [7] for a similar problem for the PGPE theory. Here we adapt the calculations for specific use for the SGPE, that is, to find the appropriate chemical potential and energy cutoff.

### 4.2.1 Chemical Potential

The chemical potential can be found by determining the condensate number for a specified number of atoms in the total system. Here we estimate this relationship using a semiclassical Hartree-Fock theory, which accounts for interactions between atoms in the system at a mean field level. This theory predicts that the density of states for energy levels above the ground state is of the form [14]

$$\rho_{\text{HF}}(\epsilon) = \int \frac{d^3\mathbf{x}d^3\mathbf{p}}{(2\pi\hbar)^3} \delta\left(\epsilon - \left[\frac{p^2}{2m} + V_{\text{trap}}(\mathbf{x}) + 2U_0n_c(\mathbf{x})\right]\right), \quad (4.1)$$

where the condensate density is given by the Thomas-Fermi approximation

$$n_c(\mathbf{x}) = \begin{cases} \frac{1}{U_0} (\mu_{\text{TF}} - V_{\text{trap}}(\mathbf{x})) & \mu_{\text{TF}} - V_{\text{trap}}(\mathbf{x}) \geq 0 \\ 0 & \mu_{\text{TF}} - V_{\text{trap}}(\mathbf{x}) < 0 \end{cases}. \quad (4.2)$$

The Hartree-Fock density of states can not in general be solved analytically, but it can easily be handled for the case of a harmonically trapped condensate as shown by Stoof *et al.* [3]. They find an analytical expression of the form

$$\rho_{\text{HF}}(\epsilon) = \frac{2}{\pi\hbar\bar{\omega}} [I_-(\epsilon) + I_+(\epsilon)], \quad (4.3)$$

where  $\bar{\omega}$  is the geometric average of the trapping frequencies,  $\bar{\omega} = (\omega_x\omega_y\omega_z)^{1/3}$ .  $I_-(\epsilon)$  and  $I_+(\epsilon)$  are defined by

$$I_-(\epsilon) = \frac{u_-^3x}{4} - \frac{a_-u_-x}{8} - \frac{a_-^2}{8} \log(x + u_-) \Big|_{x=\sqrt{\max\{0, a_-\}}}^{x=\sqrt{2\mu_{\text{TF}}/\hbar\bar{\omega}}} \quad (4.4)$$

$$I_+(\epsilon) = -\frac{u_+^3x}{4} + \frac{a_+u_+x}{8} + \frac{a_+^2}{8} \sin^{-1}\left(\frac{x}{\sqrt{a_+}}\right) \Big|_{x=\sqrt{2\mu_{\text{TF}}/\hbar\bar{\omega}}}^{x=\sqrt{a_+}} \quad (4.5)$$

and where  $a_{\pm} = 2(\epsilon \pm \mu_{\text{TF}})/\hbar\bar{\omega}$ , and  $u_{\pm} = \sqrt{a_{\pm} \mp x^2}$ .

By approximating atomic interactions in this way, the Hartree-Fock density of states can be used to predict the system chemical potential by finding the number of atoms in the

condensate. Since  $\rho_{\text{HF}}(\epsilon)$  treats the energy levels above the ground state, the total number of atoms in the system is given by

$$N_{\text{T}} = \int_0^{\infty} d\epsilon \rho_{\text{HF}}(\epsilon) n_{\text{BE}}(\epsilon) + N_{\text{c}}, \quad (4.6)$$

where  $N_{\text{c}}$  is the number of atoms in the Bose-Einstein condensate, not to be confused with the number in the condensate band  $N_{\text{C}}$ . We evaluate this integral numerically and find that the product  $\rho_{\text{HF}}(\epsilon) n_{\text{BE}}(\epsilon)$  is negligible for  $\epsilon \gg k_{\text{B}}T$ , so we use a value of  $15k_{\text{B}}T$  as the upper limit on the integral which gives good convergence. The number of atoms in a single energy state  $n_{\text{BE}}$ , is given by usual Bose-Einstein distribution

$$n_{\text{BE}} = \frac{1}{e^{(\epsilon-\mu)/k_{\text{B}}T} - 1}. \quad (4.7)$$

By specifying the total number of atoms in the system (4.6) can be solved approximately to give  $N_{\text{c}}$ , and hence  $\mu$ , using the Thomas-Fermi relation [14]

$$\mu = \frac{\hbar\bar{\omega}}{2} \left( \frac{15N_{\text{c}}a_{\text{s}}}{\bar{a}} \right)^{2/5}, \quad (4.8)$$

where the geometric average of oscillator frequencies is given by  $\bar{\omega} = (\omega_x\omega_y\omega_z)^{1/3}$ , the harmonic oscillator length is  $\bar{a} = \sqrt{\hbar/m\bar{\omega}}$ , and  $a_{\text{s}}$  is the s-wave scattering length. For temperatures above  $T_{\text{c}}$ ,  $\rho_{\text{HF}}$  becomes the standard single particle density of states, thus  $\mu$  can be found easily for temperatures above the transition using (4.6), where  $N_{\text{c}} = 0$ .

### 4.2.2 Energy Cutoff

C-field methods require macroscopic occupation at the cutoff energy  $\epsilon_{\text{cut}}$ . By specifying the mean occupation at the cutoff at a particular value in the range  $1 \leq n_{\text{cut}} \leq 10$ , the energy required to have this occupation can be found using (4.7). The energy origins in the Hatrie-Fock theory and c-field methods differ, so care needs to be taken to identify the value of  $\epsilon_{\text{cut}}$  for use in the SGPE. The Hatrie-Fock density of states is based on energy being measured relative to the condensate, so rearranging (4.7) with  $\mu = 0$  gives

$$\epsilon_{\text{cutHF}} = k_{\text{B}}T \ln \left( 1 + \frac{1}{n_{\text{cut}}} \right). \quad (4.9)$$

This is valid for  $T < T_{\text{c}}$ , where  $\epsilon_{\text{cutHF}}$  is the energy based on the HF density of states where the mean occupation is  $n_{\text{cut}}$  as chosen. Since  $\epsilon_{\text{cutHF}}$  is based on the energy relative to the condensate, its exact value will not be of use as a simulation parameter defining  $\epsilon_{\text{cut}}$ . However finding the number of modes based on this energy cutoff will lead to finding the correct single particle energy required for SGPE simulations. Integrating  $\rho_{\text{HF}}$  up to  $\epsilon_{\text{cutHF}}$  will give the number of single particle states

$$M_{\text{below}} = \int_0^{\epsilon_{\text{cutHF}}} d\epsilon \rho_{\text{HF}}(\epsilon). \quad (4.10)$$

The SGPE uses harmonic oscillator energy levels, so  $\epsilon_{\text{cut}}$  as a simulation parameter must be found relative to the harmonic oscillator density of states. By finding what energy is required for the harmonic oscillator density of states to give the same number of modes,  $M_{\text{below}}$  as given by (4.10),  $\epsilon_{\text{cut}}$  can be found. That is, the energy cutoff used in SGPE simulations is given by finding  $\epsilon_{\text{cut}}$  such that

$$\int_0^{\epsilon_{\text{cutHF}}} d\epsilon \rho_{\text{HF}}(\epsilon) = M_{\text{below}} = \int_{\epsilon_0}^{\epsilon_{\text{cut}}} d\epsilon \rho_{\text{HO}}(\epsilon), \quad (4.11)$$

where  $\epsilon_0$  is the ground harmonic oscillator energy, and  $\rho_{\text{HO}}$  is the harmonic oscillator density of states

$$\rho_{\text{HO}}(\epsilon) = \frac{\epsilon^2}{2(\hbar\bar{\omega})^3}. \quad (4.12)$$

For temperatures above the transition, the single particle density of states is applicable so  $\epsilon_{\text{cut}}$  can be found directly from the Bose-Einstein distribution

$$\epsilon_{\text{cutHF}} = \epsilon_{\text{cut}} = k_{\text{B}}T \ln \left( 1 + \frac{1}{n_{\text{cut}}} \right) + \mu. \quad (4.13)$$

Note that while we must solve this set of equations numerically, the relation between  $N, T, \mu(T)$ , and  $\epsilon_{\text{cut}}(T)$  can be found in a fraction of a second. This is in contrast to using SGPE simulations with the trial and error approach, where typically a single simulation takes a time of order hours.

## 4.3 Results

### 4.3.1 Hatree-Fock Results

By fixing the total number of atoms in the system, for a given temperature the Hatree-Fock calculations give a quick way to estimate both the chemical potential and the energy cutoff. Figure 4.1 shows the results of the Hatree-Fock calculations for a system based on an axisymmetric trap  $\omega_r = 2\pi \times 8$  and  $\omega_z = 15\omega_r$ , containing  $2 \times 10^6$  total atoms. The figure shows the chemical potential and energy cutoff based on 4 different occupations at the cutoff, calculated using the methods described above. SGPE simulations require that  $\epsilon_{\text{cut}}$  be at least twice the size of  $\mu$  to prevent any cutoff problems in the numerics. It can be seen that  $\epsilon_{\text{cut}}$  based on using  $n_{\text{cut}}$  of 1 or 2 gives plenty of headroom over the temperature range of interest for SGPE simulations, that is, in high temperature regimes (usually in the range  $0.7T_c < T \sim T_c$ ). The Hatree-Fock calculations map over the transition temperature nicely where the Hatree-Fock theory becomes that of the ideal gas. It should be noted that the only dependence on the trapping frequencies is on  $\bar{\omega}$ . This means the calculations of the predicted parameters are independent of geometry, and can be applied to any harmonically trapped system.

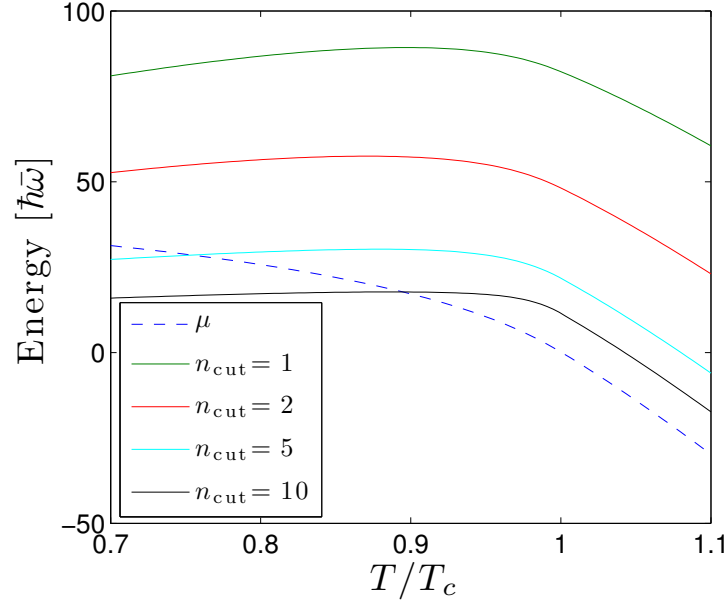


Figure 4.1: Estimated parameters  $\mu$  and  $\epsilon_{\text{cut}}$  as a function of input temperature for various values of  $n_{\text{cut}}$ , aiming for a fixed total number of  $2 \times 10^6$  atoms. Calculations for a system with an axisymmetric trap with  $\omega_r = 2\pi \times 8$ ,  $\omega_z = 15\omega_r$ .

### 4.3.2 SGPE Results

The parameters calculated are based on the Hartree-Fock density states which approximates interactions between atoms in the system. One would expect SGPE simulations to give slightly different results to these Hartree-Fock calculations. However this difference may be small enough that the approximation leads to a good estimate of parameters. The parameters chosen will be satisfactory if

1. The chemical potential found from specifying the total number of atoms at a specific temperature leads to the same total number of atoms found in the SGPE simulation at equilibrium.
2. The occupation at the cutoff is the same as that chosen to set the parameter of the energy cutoff.

#### Finding the total number of atoms

The total number of atoms from a SGPE simulation can be found from

$$N_{\text{T}} = N_{\text{C}} + N_{\text{NC}}, \quad (4.14)$$

where  $N_{\text{C}}$  refers to the mean number of atoms in the condensate band. The number of



particles in the condensate band is found simply by using the classical field wave function (3.34)

$$N_{\mathbf{C}} = \int d^3\mathbf{x} |\psi_{\mathbf{C}}(\mathbf{x})|^2. \quad (4.15)$$

In this work, the non-condensate band is treated as a thermal reservoir, where the atoms are thermalized into a Bose-Einstein distribution. Atoms above the cutoff primarily reside at large radii and hence are largely insensitive to interactions with condensate band atoms. The dominant effect of interactions is included in the Thomas-Fermi chemical potential, thus for atoms in an ideal Bose-Einstein distribution above the cutoff, we can write  $N_{\text{NC}}$  as [11]

$$N_{\text{NC}} = g_3(e^{\beta\mu}, \beta\epsilon_{\text{cut}})/(\beta\hbar\bar{\omega})^3, \quad (4.16)$$

where the incomplete Bose-Einstein function is defined as

$$g_\nu(z, y) \equiv \frac{1}{\Gamma(\nu)} \int_y^\infty dx x^{\nu-1} \sum_{l=1}^\infty (ze^{-x})^l = \sum_{l=1}^\infty \frac{z^l}{l^\nu} \frac{\Gamma(\nu, yl)}{\Gamma(\nu)}, \quad (4.17)$$

where  $\Gamma(\nu, x) \equiv \int_x^\infty dy y^{\nu-1} e^{-y}$  is the incomplete gamma function. So 4.16 gives the number of atoms of a non-interacting gas obeying the Bose-Einstein distribution at energies above the energy cutoff  $\epsilon_{\text{cut}}$ .

### Finding the mean occupation at the cutoff

The mean occupation at the cutoff can be found easily using the amplitudes of the classical field (3.34),  $\alpha_i$ . The average occupation of the  $i$ th single particle mode  $\phi_i(\mathbf{x})$  can be found by

$$n_i = \frac{1}{N} \sum_{n=1}^N |\alpha_i(t_n)|^2, \quad (4.18)$$

where  $N$  is the number of samples used in the time averaging. For a consistently chosen cutoff, the interacting energy eigenmodes at the cutoff  $\epsilon_{\text{cut}}$  are to a good approximation single particle states. This means the occupation at the cutoff can be found directly from (4.18) by finding the lowest value of the occupation when considering all the modes in the classical field, as the classical field is defined using single particle states as a basis (3.34).

### SGPE Simulations

SGPE simulations were run for systems of different geometry and for different targeted total atom numbers to check the estimated parameters at finite temperature and equilibrium. The parameters of chemical potential and energy cutoff were calculated over a range of temperatures using the methods above. The chosen occupation at the cutoff was two atoms per mode, as from figure 4.1 it can be seen this gives enough headroom between  $\mu$  and  $\epsilon_{\text{cut}}$  so the numerical methods are not compromised.

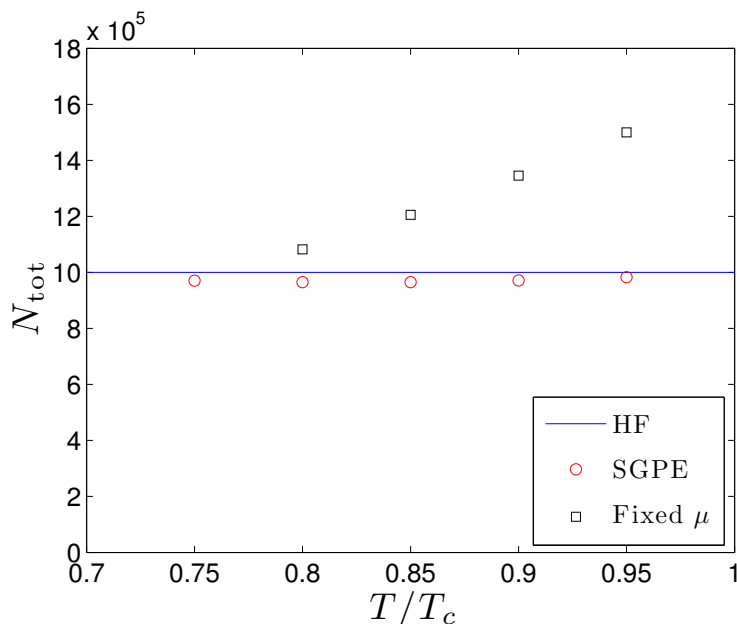


Figure 4.2: Total number of atoms in the system as a function of temperature for a spherical system with a radial trapping frequency of  $\omega_r = 2\pi \times 10 \text{ s}^{-1}$ . (blue) We use an input value of  $1 \times 10^6$  atoms in the parameter calculations. (red circle) SGPE simulations show the total atom number found with SGPE agrees well with the initial choice. (black square) Holding  $\mu$  constant and just increasing temperature as SGPE parameters results in poor agreement between the total atom number found from simulations and the initial choice.

Firstly we looked at the SGPE results for a condensate in a spherical trap with trapping frequency  $\omega_r = 2\pi \times 10 \text{ s}^{-1}$ , where the total number used in the parameter calculations was set at  $N_{\text{tot}} = 1 \times 10^6$  atoms. Figure 4.2 shows the SGPE results for the calculation of  $N_T$  for a range of temperatures. The results show that the estimated parameters lead to the SGPE giving the total number of atoms to good agreement with the fixed initial condition. There is good agreement over all temperatures but it should be noted that the total number from the SGPE is slightly less than the initial value. This means that the critical temperature of the system is slightly less than that used in the calculation of the parameters, so the actual temperature of the system is slightly higher relative to  $T_c$  than that used as an input into the SGPE simulation. The actual critical temperature of the condensate can be found easily using the general result [14]

$$k_B T_c = 0.94 \bar{\omega} \hbar N_T^{1/3}. \quad (4.19)$$

Note that although (4.19) is the ideal gas result, it gives a good approximation for our purposes. Table 4.1 shows that the temperature found from SGPE simulations is in good agreement with the initial input, hence the choice of chemical potential enables good control of temperature.

Figure 4.2 also shows the effect of holding  $\mu$  constant and just increasing temperature.

|                   |      |      |      |      |      |
|-------------------|------|------|------|------|------|
| $T/T_c$ as input  | 0.75 | 0.80 | 0.85 | 0.90 | 0.95 |
| $T/T_c$ from SGPE | 0.76 | 0.81 | 0.86 | 0.91 | 0.96 |

Table 4.1: Comparison of input temperatures and calculated temperature of system from SGPE simulations for a spherical system with  $\omega_r = 2\pi \times 10 \text{ s}^{-1}$  predicting  $N_{\text{tot}} = 1 \times 10^6$  atoms.

|                                       |      |      |      |      |      |
|---------------------------------------|------|------|------|------|------|
| $T/T_c$ as input                      | 0.75 | 0.80 | 0.85 | 0.90 | 0.95 |
| $T/T_c$ from SGPE with constant $\mu$ | 0.76 | 0.78 | 0.80 | 0.82 | 0.83 |

Table 4.2: Comparison of input temperatures and calculated temperature of system from SGPE simulations with  $\mu$  held constant for a spherical system with  $\omega_r = 2\pi \times 10 \text{ s}^{-1}$  predicting  $N_{\text{tot}} = 1 \times 10^6$  atoms.

The chemical potential is chosen via the parameter calculation for the lowest temperature and then held constant at that value for the whole range of temperatures. This results in the number of atoms in the system increasing over temperature which means the critical temperature will also increase due to (4.19). This can be seen in table 4.2 which shows simply increasing the input temperature for fixed  $\mu$  leads to no control over the resulting system temperature.

We also looked at a flattened geometry where the trapping frequency in the  $z$  direction was increased to create a pancake like condensate. We set the trapping frequencies to be  $\omega_r = 2\pi \times 8 \text{ s}^{-1}$  and  $\omega_z = 15\omega_r$ , where the total number of atoms was initially set as  $N_{\text{tot}} = 2 \times 10^6$  atoms. Figure 4.3 shows the resulting number of total atoms from the SGPE simulations using the estimated parameters for a range of input temperatures. As with the previous test the total number of atoms agrees well with the initial value, showing that the calculated parameters give good control over total number and hence temperature. This also shows the calculations will be valid for any particular choice of geometry provided the system remains three dimensional.

Figure 4.4 shows the mean occupation of the least occupied modes in the condensate band found using (4.18) for the same axisymmetric system. The atom number in the least occupied mode will be the occupation of the highest energy single particle mode, or the occupation at the cutoff  $\epsilon_{\text{cut}}$ . In this case we see that although the occupation at the cutoff is less than two as set to determine the choice of parameters, it is still much larger than one. This result shows that macroscopic occupation at the cutoff as required by the SGPE is achieved by choosing an initial value for the occupation of two.

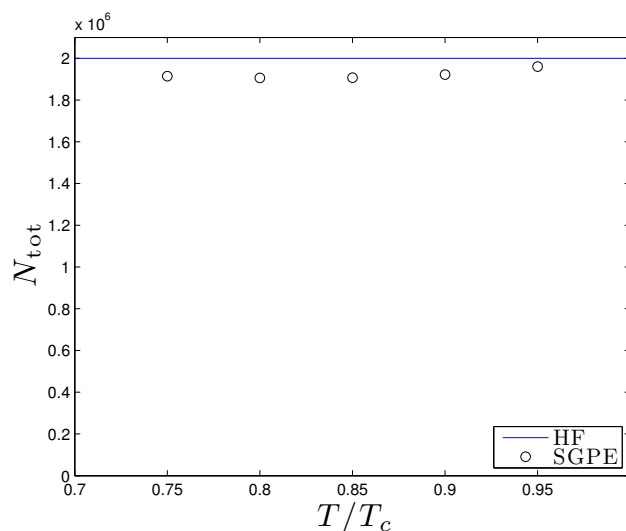


Figure 4.3: Total number of atoms in the system as a function of temperature for an axisymmetric trapping potential,  $\omega_r = 2\pi \times 8 \text{ s}^{-1}$  and  $\omega_z = 15\omega_r$ . (blue) The initial choice of the total atom number is  $2 \times 10^6$  atoms. (black circle) Total atom number found from SGPE simulations agrees well with the initial choice, but note the agreement is not as good as for the symmetrically trapped system (figure 4.2).

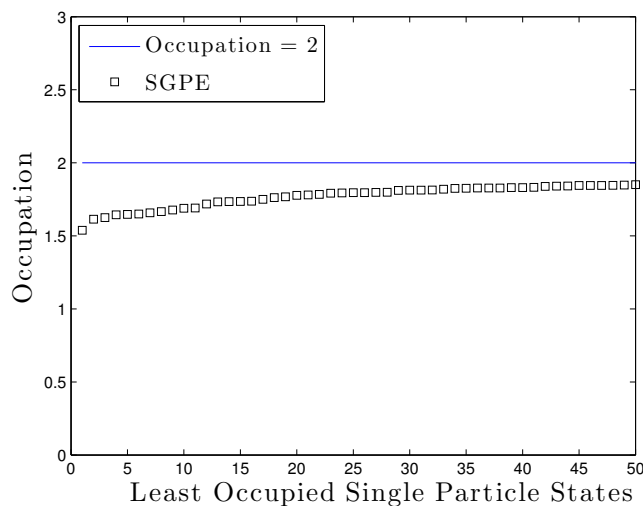


Figure 4.4: Occupation number of the 50 least occupied single particle energy modes. Simulation parameters are the same as mentioned in figure 4.3, and based on  $n_{\text{cut}} = 2$  (blue line). We see the smallest occupation is greater than 1.5 so the occupation at the energy cutoff will be larger than one, thus the occupation criteria for the SGPE is satisfied.

## 4.4 Limitations

Although the total number of atoms found from SGPE simulations agrees to more than 95% with the initial choice, figures 4.2 and 4.3 show that there is greater agreement with the spherical system. The difference between the spherical and 15:1 geometry here is minimal. However this is a problem when the aim is to compare different geometries at the same temperature, as the actual temperature of the corresponding systems may be slightly different. This slight difference is a byproduct of using the Hartree-Fock approximation and is a limitation on the choice of parameters. However as the difference in the total number of atoms is minimal, we use the parameters found directly from these methods even though the SGPE relative temperature is slightly different across geometry. This difference is clear in our results (see figure 6.9) where different data sets have slightly different relative temperatures.

## 4.5 Summary

The methods to estimate SGPE parameters shown here, using calculations involving the Hartree-Fock approximation, has provided a quick and efficient way to choose suitable simulation parameters to control atom number. These calculations mean parameters can be chosen such that the temperature of the system can be controlled, and that the occupation at the cutoff is large enough for the SGPE to be valid. The importance of these calculations should not be undervalued despite the simplicity of the method. In some studies mapping out an effective parameter space has consisted of checking hundreds of simulations where the parameters have been finely adjusted. Our method avoids such a time consuming process and gives good SGPE parameters in a matter of seconds. We expect this tool will be widely used by others performing SGPE simulations and, since SGPE equilibria are also very close to PGPE equilibria, it can be used for microcanonical simulations also.

SGPE simulations show that the parameters chosen give a slightly lower total number of atoms than the value chosen in the Hartree-Fock calculations. This is expected as the Hartree-Fock method is just an approximation of the interactions between atoms, and it is unlikely that it would describe the system exactly. Despite this, the control over the system given by these calculations is more than adequate to be confident in applying the SGPE to a study of high temperature Bose-Einstein condensates over a range of temperatures and geometries.

# Chapter 5

## Numerical Methods

The main aim of this research is to investigate the physics of high temperature Bose-Einstein condensation predicted by the simple growth SGPE

$$\begin{aligned} (S)d\psi_{\mathbf{C}}(\mathbf{x}, t) &= \mathcal{P}_{\mathbf{C}} \left\{ -\frac{i}{\hbar} \left( H_{\text{sp}} + u|\psi_{\mathbf{C}}(\mathbf{x}, t)|^2 \right) \psi_{\mathbf{C}}(\mathbf{x}, t) dt \right. \\ &\quad \left. + \frac{\gamma}{k_{\text{B}}T} \left[ \mu - \left( H_{\text{sp}} + u|\psi_{\mathbf{C}}(\mathbf{x}, t)|^2 \right) \right] \psi_{\mathbf{C}}(\mathbf{x}, t) dt + dW_{\gamma}(\mathbf{x}, t) \right\}. \end{aligned} \quad (5.1)$$

The numerical methods behind the simple growth SGPE (5.1) are not trivial and years of research has been spent finding a method of solution. The methods used to solve (5.1) are based on the numerical solution to the PGPE (3.46), as the only difference between these two equations is the damping and additive noise which are numerically easy to deal with. The theory behind the PGPE numerical methods of solution were formulated by Blakie and Davis [4, 6], details of which are not important to this project.

Here we outline how we create a vortex state numerically within the SGPE framework and state how we detect the vortex while coping with thermal fluctuations, which make tracking the vortex more difficult than in the zero temperature Gross-Pitaevskii case. We consider numerical convergence, and also give details of the parameters used to investigate vortex dynamics in different regimes.

### 5.1 Vortex States

The first step in constructing a vortex state in a Bose-Einstein condensate is to find an equilibrium ground state to which a vortex can be phase imprinted onto. This equilibrium state can be found by simply letting an initial random state undergo SGPE evolution for a long enough time, where the length of time needed is set by the damping rate  $\gamma$ . Hence a large value of  $\gamma$  will lead to an equilibrium state occurring after a shorter time proportional to  $1/\gamma$ . We further decrease the time needed to create an equilibrium state using a Thomas-Fermi

ground state with density [14]

$$n_c(\mathbf{x}) = \begin{cases} \frac{1}{U_0} (\mu_{\text{TF}} - V_{\text{trap}}(\mathbf{x})) & \mu_{\text{TF}} - V_{\text{trap}}(\mathbf{x}) \geq 0 \\ 0 & \mu_{\text{TF}} - V_{\text{trap}}(\mathbf{x}) < 0 \end{cases}. \quad (5.2)$$

Using this density as the initial state gives a close representation of the eventual equilibrium state, hence the evolution to equilibrium will be faster than other choices.

Once an equilibrium state is found, a vortex state can be made simply by multiplying the wave function by a spatially dependent phase. Formally, the vortex phase is imprinted by

$$\hat{\psi}_{\mathbf{C}}(\mathbf{x}) = \hat{\psi}'_{\mathbf{C}}(\mathbf{x}) \exp[i\Theta(\mathbf{x})], \quad (5.3)$$

where  $\hat{\psi}'_{\mathbf{C}}(\mathbf{x})$  is the wave function representing the equilibrium ground state. The phase factor is defined as

$$\Theta(\mathbf{x}) = \tan^{-1} \left[ \frac{y - y_0}{x - x_0} \right], \quad (5.4)$$

which is the phase profile associated with a single straight vortex at position  $(x_0, y_0)$ , so the vortex is aligned perpendicular to the  $x - y$  plane, or along the  $z$  axis. We investigate the dynamics of a centrally located vortex, so  $(x_0, y_0) = (0, 0)$ .

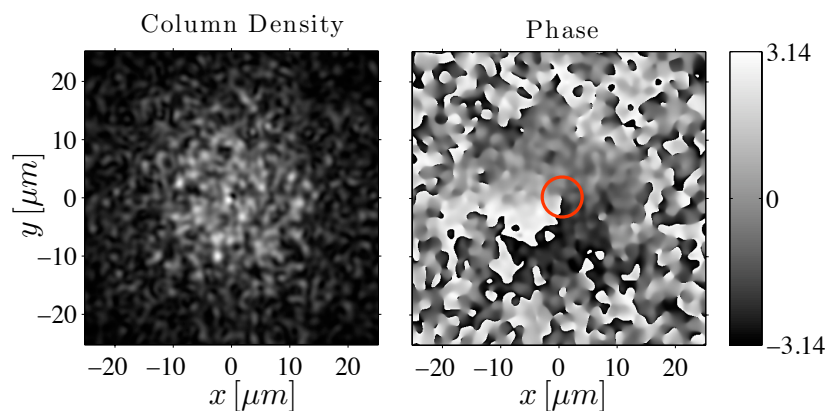
## 5.2 Vortex Detection

The task of detecting a vortex poses a challenge when using the SGPE due to the noise which creates density and phase fluctuations. Our aim is to find a quick and efficient method to locate the vortex so we could not only measure the vortex lifetime, but also its radius as time evolves. In a zero temperature Bose-Einstein condensate with a vortex located at  $\rho = (x, y)$  in the  $x$ - $y$  plane, the curl of the velocity flow is a pure delta function [35]

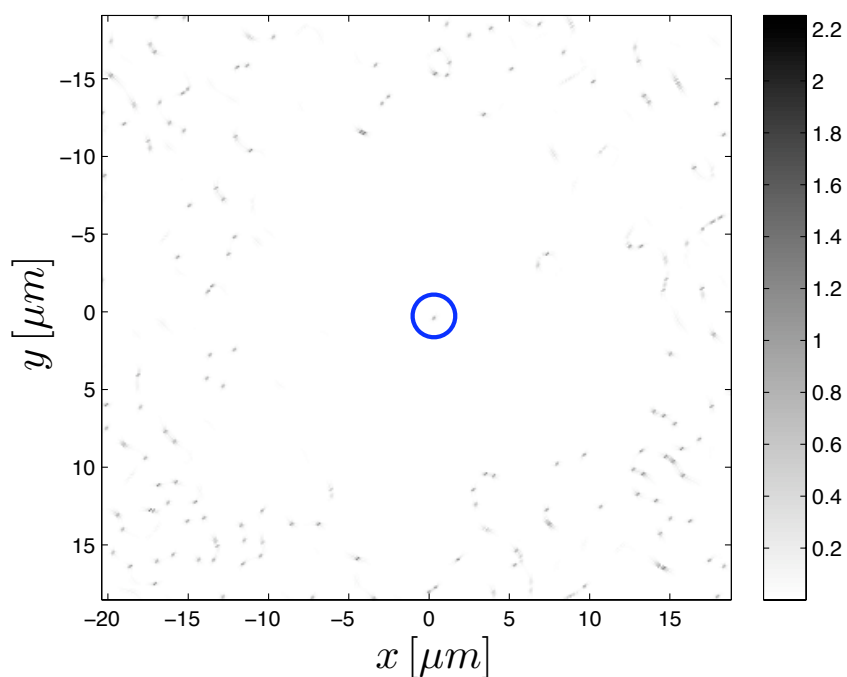
$$\nabla \times \mathbf{v} \propto \delta^2(\rho). \quad (5.5)$$

However at finite temperature using the SGPE, fluctuations introduced by the stochastic noise leads to a more complicated picture. Figure 5.1 shows a typical image from a SGPE simulation (figure 5.1(a)) along with the associated curl of the velocity field (figure 5.1(b)). We observe that the curl not only shows a signal at the position of the vortex, but also outside the condensate due to thermal fluctuations.

These extra fluctuations are primarily based in regions of space of radius larger than the actual condensate, which makes the curl signal from the vortex very obvious. Hence by masking all the extra fluctuations the vortex can be found very easily in the area of relevance.



(a) Column density and phase slice of a single vortex. Vortex most easily observed by the phase singularity (red circle).



(b) Curl of the velocity where the magnitude of the curl is given by the color gradient. The signal corresponding to a single vortex is labeled by the blue circle.

Figure 5.1: Image of the column density and phase (a) of a single vortex in a system with a 4:1 geometry at  $T/T_c = 0.93$ , as well as the curl of the velocity field (b) showing the effects of phase fluctuations.



### 5.3 Mean First Exit Time

When looking at vortex lifetimes over a range of parameters, it is important to define the lifetime relative to a suitable radius. As mentioned in section 5.2, we can only clearly detect the vortex when the thermal fluctuations near the boundary are masked. We use an initial circular mask to mask out fluctuations at the boundary, with radius equal to the Thomas Fermi radius. However as at finite temperature the actual condensate radius becomes smaller, and as the random fluctuations may appear slightly inside the actual condensate, we use an adaptive circular mask. We use this to define the radius by detecting the vortex in individual SGPE simulation saves as follows:

1. We detect the vortex by looking for the position where the curl of the velocity field is maximum. We start with a centrally located vortex, hence if our detection finds the largest curl signal at the center we accept that it has found the vortex. Otherwise, we incrementally reduce the radius of the circular mask until it registers that the center of the condensate is the position where the curl is maximum. We keep this new mask radius when looking at the next SGPE save.
2. As the thermal fluctuations are random, they may encroach this new mask radius we have set. To cope with this, we use the fact that we know that the vortex will generally follow some spiral like trajectory to the condensate boundary. Thus we would expect little deviation in the vortex radius from its position in subsequent SGPE simulation saves. With this in mind, we set some tolerance which sets the maximum change in radius of the vortex which will be acceptable between SGPE saves. If the change in location of the maximum curl lies within this tolerance, we accept the position as the vortex position. Otherwise we again reduce the mask radius incrementally until this condition is satisfied.
3. We continue the process specified in 2, until there there is no signal generated by the curl. The radius of the last valid vortex position is defined as the radius of the condensate which we measure the vortex to, which is the radius at which the vortex becomes indistinguishable from fluctuations. We define the *mean first exit time* as the time taken for the vortex to reach this radius.

Using this detection scheme means that finding the mean radius of the vortex needs to be done with caution, due to the fact that some trajectories will show a shorter vortex lifetime than others. Figure 5.2 shows the different lifetimes found for each trajectory using this mean first exit time approach and the corresponding radius at each time. We see that for the colder system at  $T/T_c = 0.78$  there is not that much variation in the vortex exit times for each trajectory. In contrast, the system at  $T/T_c = 0.93$  shows the exit time varies greatly due to the increased fluctuations. In calculating the mean radius we assume that once the vortex has become unobservable for a single trajectory, the vortex radius remains constant at the radius of its last defined position. This ensures that we will have a well defined ensemble mean even if some trajectories have very short vortex lifetimes. Making this assumption

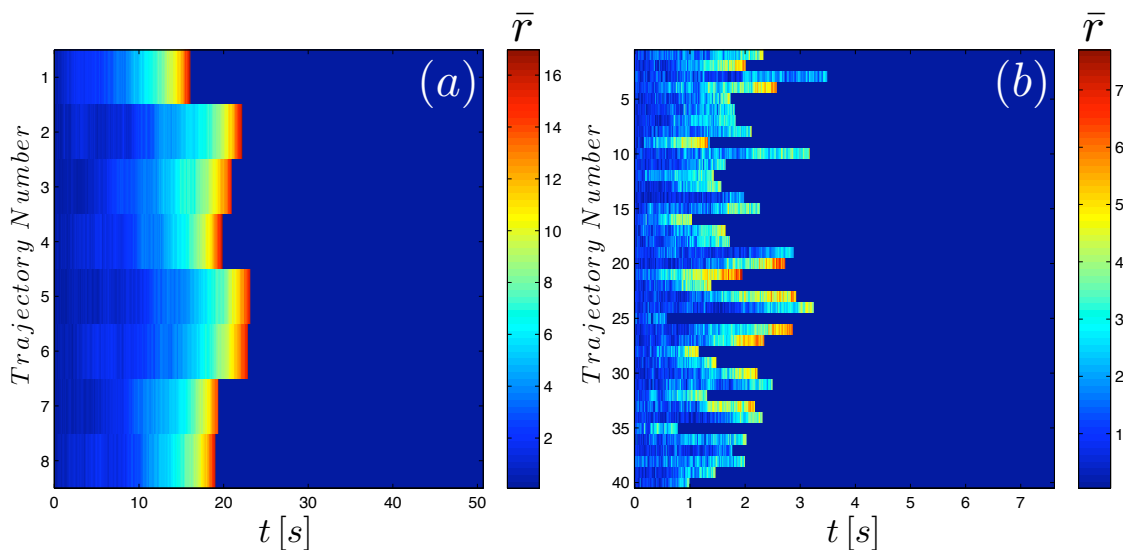


Figure 5.2: Images showing the radius of a single vortex from the centre of the condensate for each individual trajectory as a function of time for (a)  $T/T_c = 0.78$ , and (b)  $T/T_c = 0.93$ . The radius (in units of  $\mu m$ ) is shown by the color gradient, where the region which is zero after the radius reaches its maximum value represents a vortex free condensate. Note in the hotter case (b), there is large variation in the radius of the vortex at the exit time.

means the mean radius will only correspond to a real physical value for times such that the majority of trajectories still have an observable vortex position. Hence we only consider the mean vortex radius for a time less than the mean first exit time.

## 5.4 Convergence

The numerical method behind solving the simple growth SGPE (5.1) uses a pseudospectral adaptive Runge-Kutta method in the interaction picture [8, 15]. We do not address the many subtleties of stochastic convergence here, but rather choose a small tolerance and reduce it to check convergence. The error in each time step in the adaptive Runge-Kutta method is found by comparing a fourth and fifth order accurate estimate for the solution, where the time step is accepted if the error is less than the chosen tolerance. We use a tolerance of  $10^{-6}$ , and compared this with a tolerance of  $5 \times 10^{-7}$ . Figure 5.3 shows that halving our initial tolerance value does not change the convergence of a typical angular momentum decay curve. Note that we checked this tolerance by averaging 40 trajectories corresponding to a temperature of  $T/T_c = 0.93$ , the hottest temperature we consider. Since at this temperature the variation in single trajectories is largest, we use a tolerance of  $10^{-6}$  for all other regimes based on this result.

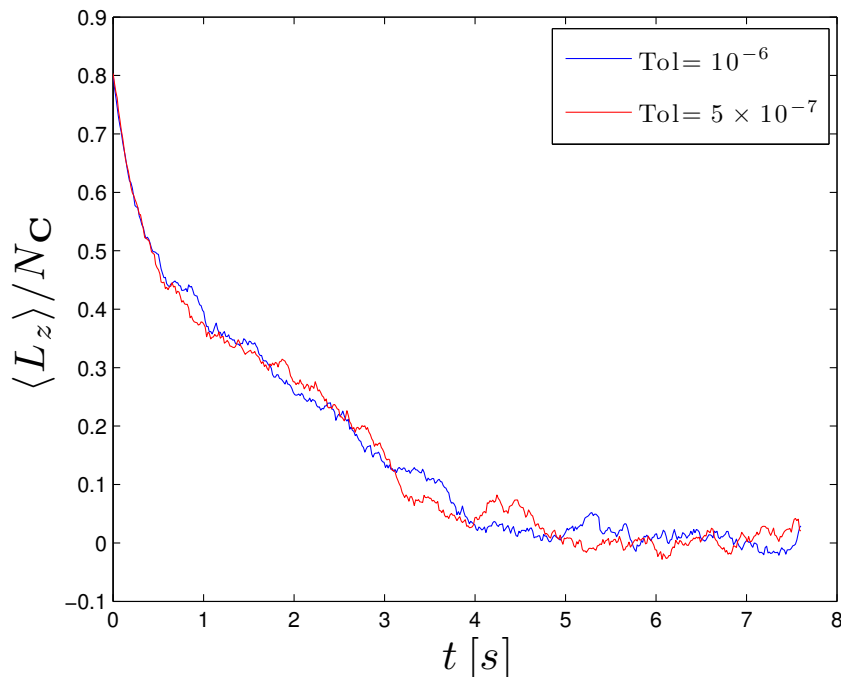


Figure 5.3: The decay of angular momentum found from an average of 40 trajectories for a tolerance of  $10^{-6}$  (blue), and  $5 \times 10^{-7}$  (red), for a system at  $T/T_c = 0.93$  with an aspect ratio of 4:1, with  $\bar{\omega}$  set by (5.6). For this high temperature where fluctuations are significant, the two different tolerance values lead to the same averaged angular momentum decay so we use a tolerance of  $10^{-6}$  for all temperatures.

## 5.5 Simulation Parameters

We investigate the stability and dynamics of a single vortex in a high temperature Bose-Einstein condensate over a range of temperatures and geometries. As the dimensions of the system are set by  $\bar{\omega}$ , we keep the geometric mean constant while adjusting the aspect ratio of the harmonic trapping potential. In all cases we calculate  $\mu$  and  $\epsilon_{\text{cut}}$  using the calculations described in chapter 4, based on input values of  $5 \times 10^5$  total atoms in the system and a cutoff occupation of two. The fixed parameters for all simulations are the total number of atoms and  $\bar{\omega}$ , while  $\mu$  and  $\epsilon_{\text{cut}}$  are constant for a specific temperature over all aspect ratios considered.

The damping rate  $\gamma$  is calculated using (3.54), and as it depends on  $T$ ,  $\mu$  and  $\epsilon_{\text{cut}}$ , it will also be constant for a given temperature over all aspect ratios considered.

The varied parameters are the aspect ratio and temperature. We consider four different geometries ranging from highly axisymmetric to purely spherical. The aspect ratios investigated are 15:1, 4:1, 2:1 and 1:1, where the ratios are given in the form  $\omega_z:\omega_r$ . The geometric

|  |       |       |       |       |       |       |       |
|--|-------|-------|-------|-------|-------|-------|-------|
| $T/T_c$ as input                           | 0.77  | 0.80  | 0.83  | 0.85  | 0.88  | 0.90  | 0.92  |
| $\mu[\hbar\bar{\omega}]$                   | 16.13 | 15.06 | 13.85 | 12.94 | 11.39 | 10.19 | 8.83  |
| $\epsilon_{\text{cut}}[\hbar\bar{\omega}]$ | 34.45 | 35.03 | 35.47 | 35.66 | 35.76 | 35.67 | 35.39 |
| $\gamma\hbar/k_B T [10^{-4}]$              | 7.11  | 6.91  | 6.76  | 6.68  | 6.57  | 6.52  | 6.49  |
| No. of trajectories                        | 8     | 10    | 10    | 10    | 20    | 20    | 40    |

Table 5.1: Simulation parameters used in SGPE simulations and the number of trajectories found for each temperature regime for a single dimensionality. We look at four geometries with aspect ratios of 15:1, 4:1, 2:1 and 1:1, with  $\bar{\omega}$  set by (5.6). As we look at multiple geometries, the total number of trajectories required becomes very large.

average is set from the 15:1 geometry where we set  $\omega_r = 2\pi \times 8$ , so

$$\bar{\omega} = ([2\pi \times 8]^2 \times 15(2\pi \times 8))^{1/3} = 2\pi \times 19.73 \text{ s}^{-1}. \quad (5.6)$$

This value of  $\bar{\omega}$  will be used for all simulations, so the values of each individual trapping frequency for a particular dimensionality is found from  $\bar{\omega}$ .

For each dimensionality the vortex dynamics over seven temperatures are investigated, using temperatures ranging from  $0.77T_c$  to  $0.92T_c$  as inputs into the SGPE parameter calculations. All the parameters used in this investigation are listed in table 5.1.

## 5.6 Computational Requirements

The SGPE theory is a purely stochastic theory based on Wigner formalism. This means although single trajectories give results which have a physical interpretation as a single experimental realization, to truly understand the overall dynamics of a single regime we average over a suitable ensemble of trajectories. In section 6.2 we find the role temperature has in the rate of statistical convergence. Based on these results from section 6.2, we performed over 450 individual trajectories (see trajectory numbers in table 5.1). This numerical investigation was very computationally intensive where simulation times ranged from one day for the hottest cases to more than one week for the coldest regime. The total computing time used in this work to amass an acceptable number of trajectories is estimated at approximately four years.

# Chapter 6

## Results

In this chapter we present the results of investigating single vortex dynamics at high temperature using the SGPE. We use the parameters as specified in section 5.5 to investigate the influence temperature and geometry have on the decay of a single vortex.

We present observations of finite vortex lifetime based on single SGPE trajectories. We use ensemble averaging to calculate the angular momentum decay and mean radius of a single vortex originating at the center of the condensate. This is compared with the mean first exit time as defined in section 5.3. We perform an extensive numerical study over a range of temperatures and geometries and look for the effect of these parameters on vortex decay.

Broadly speaking, there are two kinds of decay process we wish to distinguish:

- (a) Purely dissipative decay, and
- (b) Diffusive decay.

We associate (a) with evolution from a damped Gross-Pitaevskii equation with no noise, while (b) corresponds to decay activated by thermal fluctuations through noise. We determine the effect of each type of decay on the vortex motion.

### 6.1 Observation of Lifetime

We first investigated the role thermal fluctuations have in causing any vortex instability by looking for a finite vortex lifetime. Figure 6.1 shows the evolution of a single vortex in a condensate with a total atom number of  $5 \times 10^5$  atoms and an aspect ratio of 15:1 where  $\bar{\omega} = 2\pi \times 19.73 \text{ s}^{-1}$  (see (5.6)), where images (a) - (d) and (e) - (h) correspond to temperatures of  $T/T_c = 0.78$  and  $T/T_c = 0.93$  respectively. Figure 6.2 shows similar single vortex evolution, but in a spherical system with an aspect ratio of 1:1. In all cases we image along the axis of the initial vortex (referred to as the  $z$  axis throughout this section). In both cases a finite vortex lifetime is observed showing the SGPE accounts for dissipative processes which lead to vortex decay. Even at the coldest temperature of  $T/T_c = 0.78$ , there

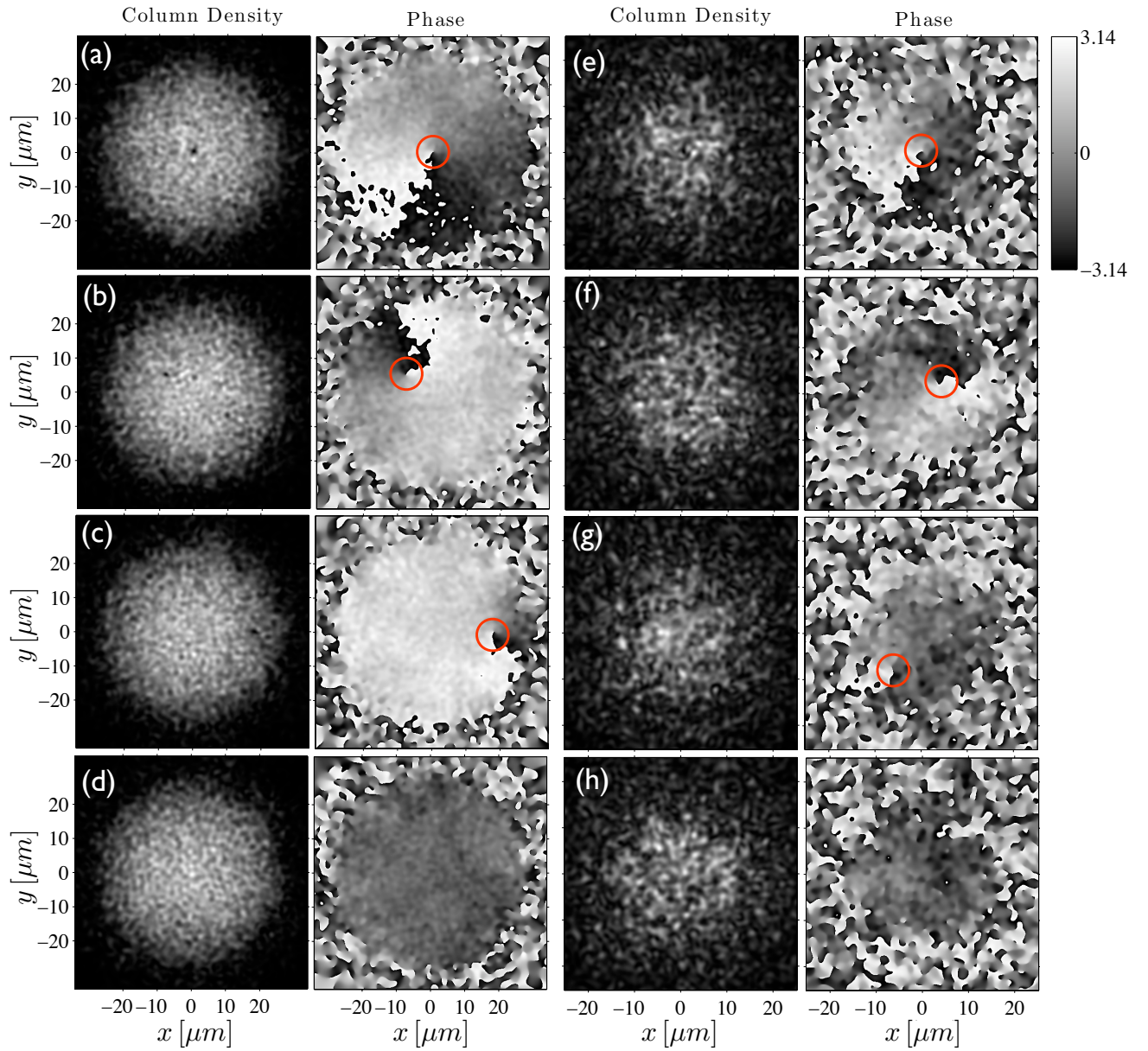


Figure 6.1: Column densities and phase slices showing vortex evolution in a system with aspect ratio of 15:1 (phase gradient top right). The vortex is best observed from the phase singularity (circle). (a)-(d): Vortex evolution for  $T/T_c = 0.78$  after  $t = 0$ ,  $\bar{\omega}t = 350 \times 2\pi$  (17.7s),  $\bar{\omega}t = 500 \times 2\pi$  (25.3s) and  $\bar{\omega}t = 580 \times 2\pi$  (29.3s), where time evolves from (a) to (d). (e)-(h): Vortex evolution for  $T/T_c = 0.93$  after  $t = 0$ ,  $\bar{\omega}t = 20 \times 2\pi$  (1.0s),  $\bar{\omega}t = 42 \times 2\pi$  (2.1s) and  $\bar{\omega}t = 45 \times 2\pi$  (2.3s), where time evolves from (e) to (h).

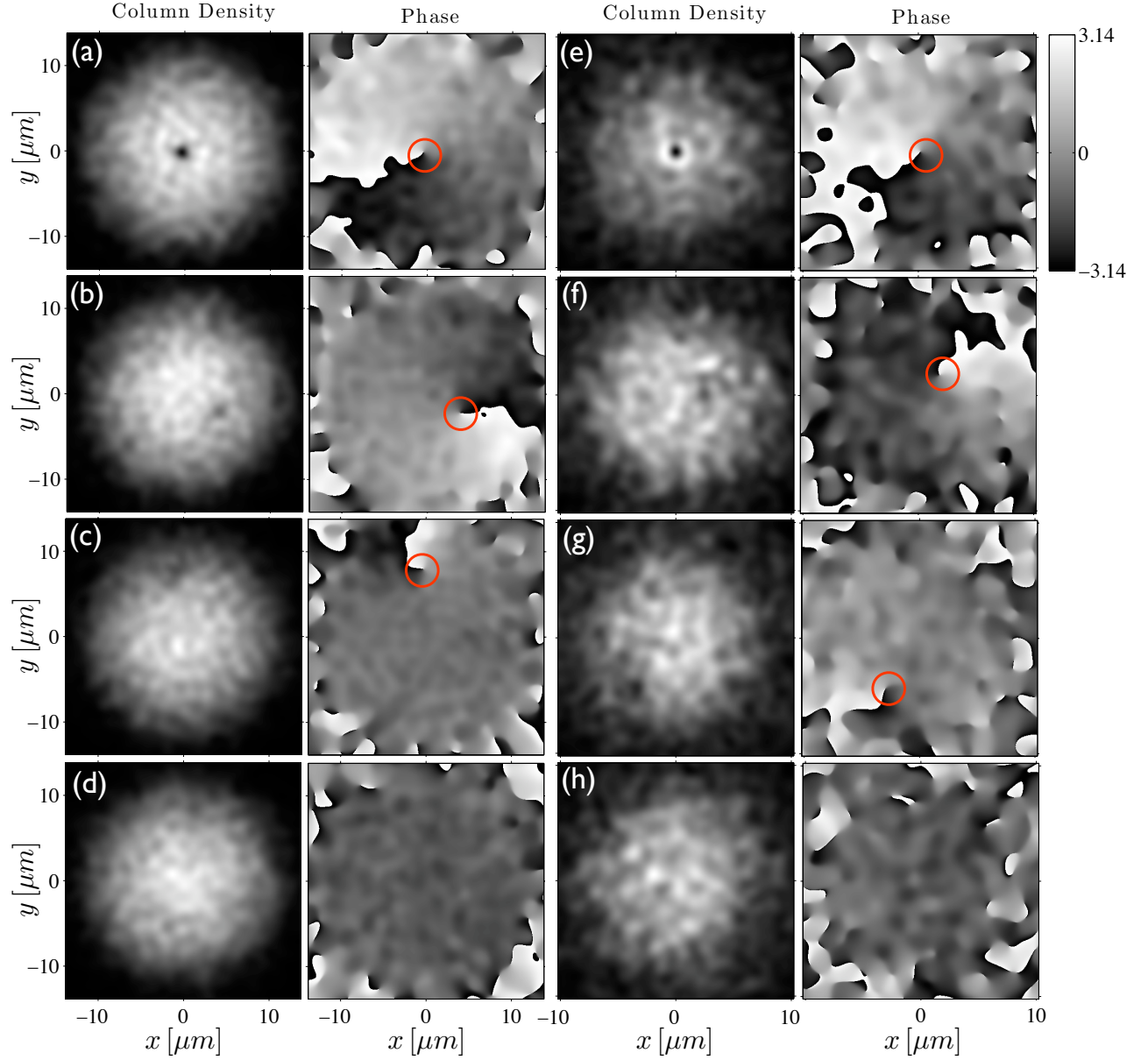


Figure 6.2: Column densities and phase slices showing vortex evolution in a spherical system with aspect ratio of 1:1 (phase gradient top right). The vortex is best observed from the phase singularity (circle). (a)-(d): Vortex evolution for  $T/T_c = 0.78$  after  $t = 0$ ,  $\bar{\omega}t = 144 \times 2\pi$  (7.3s),  $\bar{\omega}t = 180 \times 2\pi$  (9.1s) and  $\bar{\omega}t = 200 \times 2\pi$  (10.1s), where time evolves from (a) to (d). (e)-(h): Vortex evolution for  $T/T_c = 0.93$  after  $t = 0$ ,  $\bar{\omega}t = 33 \times 2\pi$  (1.6s),  $\bar{\omega}t = 42 \times 2\pi$  (2.1s) and  $\bar{\omega}t = 45 \times 2\pi$  (2.3s), where time evolves from (e) to (h).

is a substantial influence of thermal atoms presenting a pathway for dissipation to occur. However, as we elaborate below, for the colder cases the type of decay is well explained without the noise. One vital feature of the decay at all temperatures is that the initial departure of the vortex from the center is due to fluctuations, an observation which can only be seen due to the noise.

Also of note is that in both geometries at the hottest temperature of  $T/T_c = 0.93$ , the lifetime of a single vortex is much smaller than at the coldest temperature. This is expected as at higher temperature, thermal fluctuations become increasingly large causing increased instabilities to the vortex decay.

The effect of geometry on single vortex dynamics can be qualitatively seen from the column densities in figure 6.2. The initial vortex is aligned parallel with the  $z$  axis, so the vortex can be easily seen at  $t = 0$  in the column density. As time evolves we see that the vortex becomes somewhat masked in the column density due to bending of the vortex.

## 6.2 Ensemble Averaging and Statistical Convergence

As previously discussed, the SGPE is a stochastic theory where averaging of an ensemble of trajectories is necessary to quantitatively describe any observable. The single trajectory image sequences (figures 6.1 and 6.2) correspond to individual runs of experiments [5], but to understand vortex decay more deeply ensemble averaging is required.

The effect of ensemble averaging is shown in figure 6.3, where the average of the angular momentum per particle in the  $z$  direction from multiple trajectories is compared with a single realization in a system with an aspect ratio of 4:1. Figure 6.3a shows the effect of averaging eight trajectories at the coldest temperature of  $T/T_c = 0.78$ . We see that a single trajectory does tend to zero angular momentum for a vortex free condensate, but there is still noise. As at colder temperatures the effect of thermal fluctuations become less, it only takes a small ensemble of trajectories to see satisfactory statistical convergence.

This is in vast contrast to the higher temperature of  $T/T_c = 0.93$ . In figure 6.3b, we see that a single trajectory leads to a very unpredictable angular momentum curve due to the effect of fluctuations. Averaging over 10 trajectories results in smoothing out the curve but multiple random peaks due to the fluctuations are still observed. Eventually we see evidence of statistical convergence after averaging over 40 trajectories. The averaging of trajectories also leads to the angular momentum asymptotically tending to zero which represents a vortex free condensate, a fact which is unobservable from a single trajectory.

In principle one could find an arbitrarily large number of trajectories to average, leading to the greatest statistical convergence. However, due to time constraints it was not possible to find hundreds of trajectories for each regime of interest. As seen in figure 6.3, it only takes a modest number of trajectories to find nicely behaved averaged data, with the size of the ensemble more important for higher temperature. Hence we use a larger ensemble of trajectories for higher temperatures (see table 5.1).



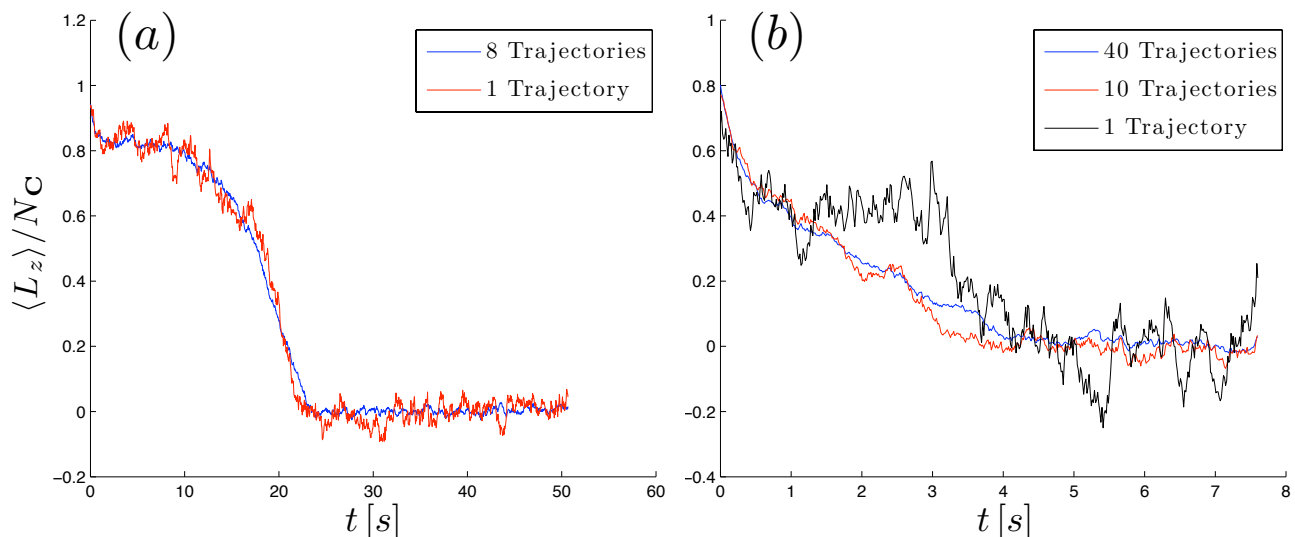


Figure 6.3: Effect of ensemble averaging single trajectories of vortex evolution. Plots of the  $z$  component of the averaged angular momentum per particle as a function of time for various ensembles of trajectories, where the condensate aspect ratio is 4:1 for  $T/T_c = 0.78$  (a) and  $T/T_c = 0.93$  (b). For reasonable statistical convergence, the hotter temperature requires a larger ensemble. Note that an angular momentum per particle of 1 corresponds to a vortex in the center of a condensate.

## 6.3 Effects of Temperature

To discuss the physical effects of temperature, we first consider the effect of temperature on single vortex dynamics in a system with a 4:1 aspect ratio with  $\bar{\omega} = 2\pi \times 19.73 \text{ s}^{-1}$ .

### 6.3.1 Angular Momentum

Figure 6.4 shows the angular momentum decay in the 4:1 system which gives a picture of the lifetime, as well as showing the different decay processes which occur at the coldest and hottest temperatures. The angular momentum per particle of a vortex free state is zero, while for a central vortex it is unity. From figure 6.4 we see that the lifetime of a single vortex decreases as the temperature increases. This is expected as at higher temperatures there is an increasing influence from the thermal cloud leading to faster decay. It is also interesting to note the vast difference in the angular momentum decay, which we will describe in detail below in section 6.3.2 using the mean first exit time. The angular momentum per particle is calculated for atoms in the condensate band as the thermal cloud has zero angular momentum in our description.

As we use ensemble averaging, we are able to calculate the standard deviation of the angular momentum. However figure 6.5 shows that the presence of a vortex hardly changes the standard deviation from its value for times when the angular momentum is zero. Thus

any variations caused by the vortex are indistinguishable from the background thermal fluctuations.

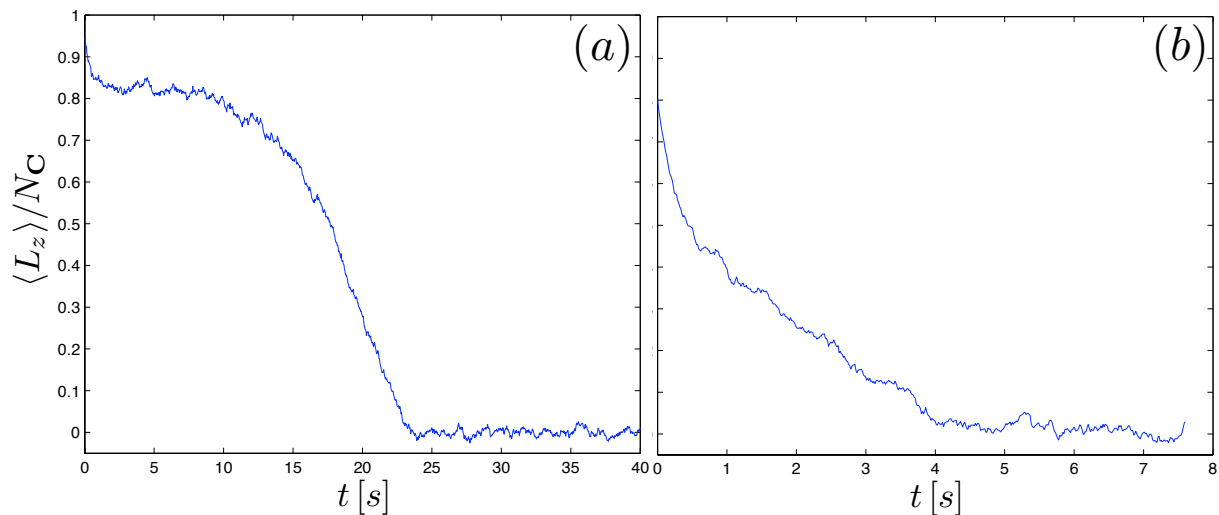


Figure 6.4: The  $z$  component of the average angular momentum per particle as a function of time in a system with a 4:1 geometry for  $T/T_c = 0.78$  (a), and  $T/T_c = 0.93$  (b). For the hotter temperature the angular momentum per particle reaches zero faster, so there is no vortex in the condensate, due to the increased influence from the thermal cloud.

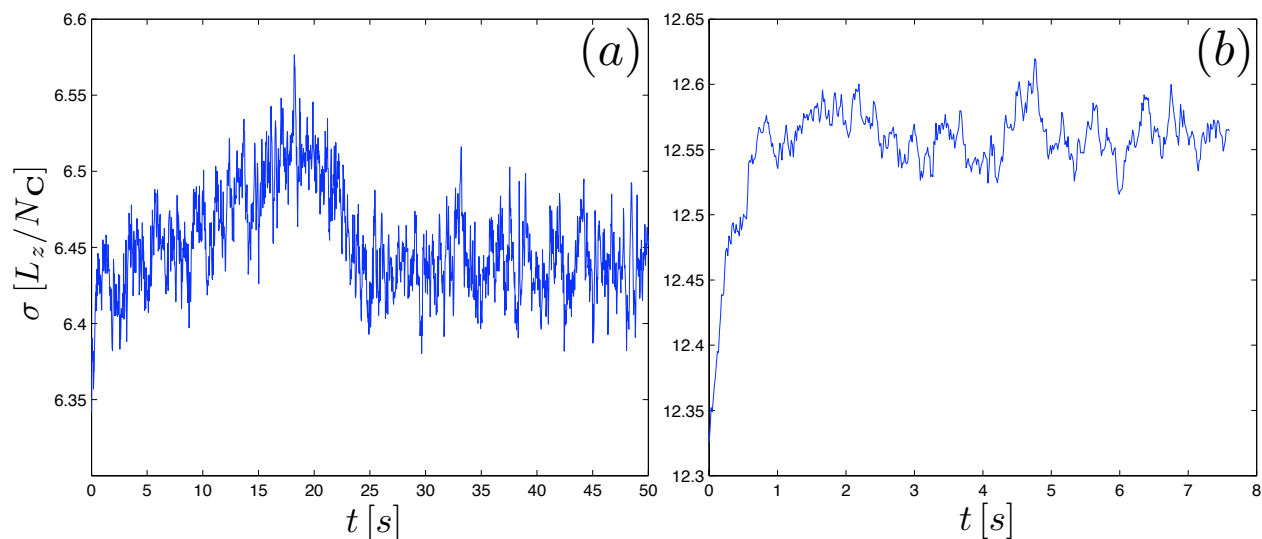


Figure 6.5: Standard Deviation of the angular momentum per particle as a function of time in a system with a 4:1 geometry for  $T/T_c = 0.78$  (a), and  $T/T_c = 0.93$  (b). The presence of a single vortex makes no significant impression over the background thermal fluctuations.

### 6.3.2 Mean First Exit Time

As in section 5.3, we define the mean first exit time as the mean time for the vortex to become indistinguishable from thermal fluctuations. Figure 6.6 shows that the mean first exit time ( $\bar{t}$ ) has an interesting linear relationship with temperature. As we define the mean first exit time based on when fluctuations make the vortex unobservable, and temperature alters the effect of fluctuations in several ways, finding such a simple linear relationship between the exit time and temperature is quite remarkable. We see the trend that  $\bar{t}$  decreases for higher temperatures, consistent with a larger thermal cloud increasing vortex instability.

Looking at the angular momentum decay and radius growth as a function of  $t/\bar{t}$  (figures 6.7 and 6.8) makes the qualitative differences in the vortex decay over temperature very clear. In figure 6.7 along with the angular momentum decay for all temperatures, we also show the decay for the case of no noise and large damping ( $\gamma = 1$ ). This is a very useful baseline as it shows the form of the angular momentum when dissipation is the only decay process prevalent. A vortex in the center of a condensate is stable and will have an infinite life time, *even with dissipation*, unless it is somehow moved from this location [23]. To find the decay curve for the case of no noise we place the initial vortex with a very slight offset. Note that  $t = \bar{t}$  corresponds well with zero angular momentum for this case of pure dissipation.

The angular momentum for the coldest temperature of  $T/T_c = 0.78$  most closely resembles the case of no noise since the effect of fluctuations are reduced at lower temperatures. For all temperatures there is an initial rapid decrease of the angular momentum which repre-

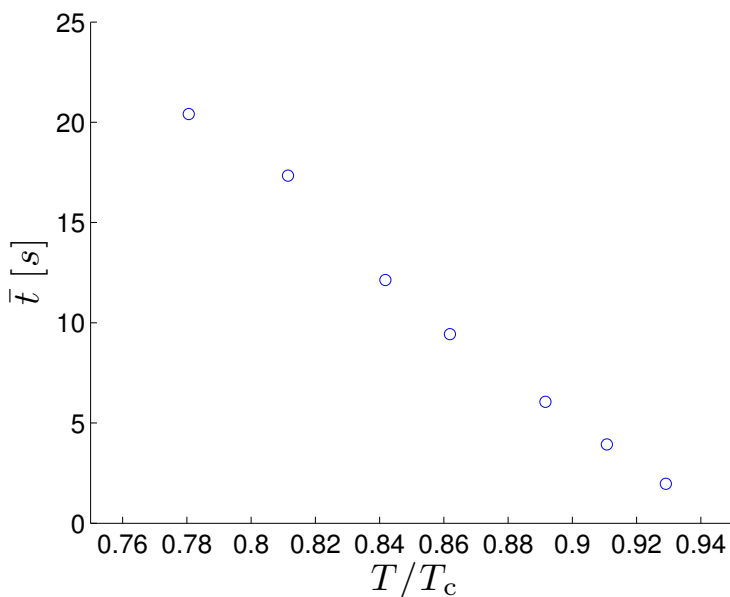


Figure 6.6: Mean first exit time of a single vortex,  $\bar{t}$ , as a function of temperature for a system with an aspect ratio of 4:1. We see a strong linear temperature dependence.

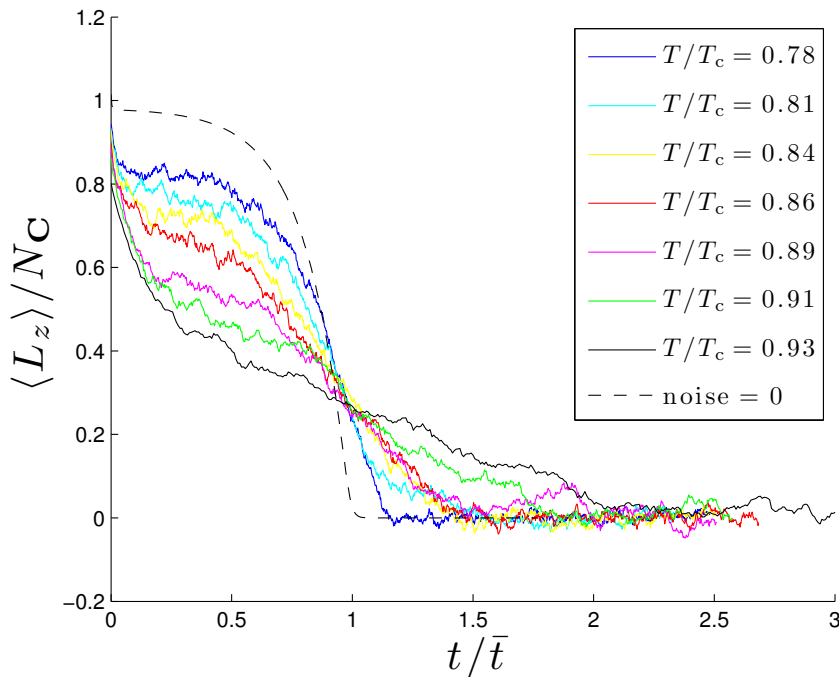


Figure 6.7: The  $z$  component of the averaged angular momentum per particle as a function of  $t/\bar{t}$ , where  $\bar{t}$  is the mean first exit time, for all temperatures in a system with an aspect ratio of 4:1 as found from an ensemble average of SGPE trajectories. The no noise case (dotted line) represents purely dissipative decay. Note the wide contrast in the form of the vortex decay where for  $T/T_c = 0.78$  we see dissipation dominating the decay, while for higher temperatures diffusive decay becomes more prevalent.

sents thermal diffusion of the vortex from its initial central position. The thermal fluctuations cause the vortex to be kicked away randomly from the center of the condensate. After this initial decay we observe that the decay is very similar to the no noise case characterized by an initially slow, then very rapid drop in the angular momentum. The rate of this drop is not as large as for the no noise case since although the fluctuations are reduced at this temperature, they are still present and clearly have some influence on vortex decay even when dissipation is the major cause of decay. As the slope of the angular momentum is very rapid at the end of the vortex decay, the time of zero angular momentum is relatively similar to the mean exit time. This is more evidence that the role of fluctuations has been suppressed leading to less variation in single SGPE trajectories.

This is in contrast to the hottest case of  $T/T_c = 0.93$  where there is a very fast initial decay of angular momentum, followed by a much slower decay as the vortex leaves the condensate. At the hottest temperature the effect of fluctuations is at its largest which leads to the initial diffusive behavior being far more pronounced, causing very rapid initial angular momentum decay of the ensemble. Subsequently the rate of angular momentum decay flattens out

considerably, continuing until the angular momentum becomes zero. The form of the angular momentum decay is completely different to the no noise case showing that diffusion caused by the effect of fluctuations dominates the vortex decay at this temperature. This creates a wide variance in mean first exit times resulting in the long slow angular momentum decay, leading to the angular momentum becoming zero at approximately twice the mean first exit time. Figure 6.7 is interesting as it shows how different the decay process of a single vortex is at high temperatures. As temperature increases from  $T/T_c = 0.78$ , the effect of fluctuations increases causing the initial diffusion to create faster angular momentum decay. After this initial diffusion there is a continuum from dissipative dominant decay for the coldest temperature to diffusion becoming more prevalent over the entire decay as temperature increases, flattening out the angular momentum curve.

We see that for all temperatures the angular momentum is tending to the same value ( $\sim 0.27$ ) near the mean first exit time. This shows that the definition of the mean first exit time is a consistent way to quantify the lifetime as it corresponds to the same angular momentum value for any temperature.

We calculate the mean radius as described in section 5.3. Figure 6.8 shows the mean radius of a single vortex agrees with these qualitative results from the angular momentum decay. Again we include the case of no noise where the mean radius increases exponentially.

Initially the early radius growth of the vortex follows the same linear increase over all temperatures. This represents the early diffusive behavior of the vortex decay and how at higher temperatures the effect of fluctuations have a larger effect. Since the condensate radius is smaller for hotter temperatures, the fact that the initial radius growth is uniform over temperature is consistent with the initial angular momentum decay becoming more rapid for higher temperatures.

After this initial universal growth, the effect of temperature becomes very apparent. Similarly to the angular momentum decay, the mean radius for  $T/T_c = 0.78$  most closely resembles the no noise case. In this case near  $t = 0.4\bar{t}$  the radius curve jumps quite dramatically, resembling the exponential growth of the no noise result. This jump shows the point where dissipative decay becomes dominant, but the underlying presence of diffusion means the curve does not become a pure exponential. In contrast, the hottest temperature of  $T/T_c = 0.93$  shows no deviation from the initial linear radius growth. This shows that diffusive based decay is most prevalent at this temperature where the effects of fluctuations are largest. Again in comparison to the angular momentum decay, we see that the SGPE shows that vortex decay over these temperatures involves a wide range of dominant processes.

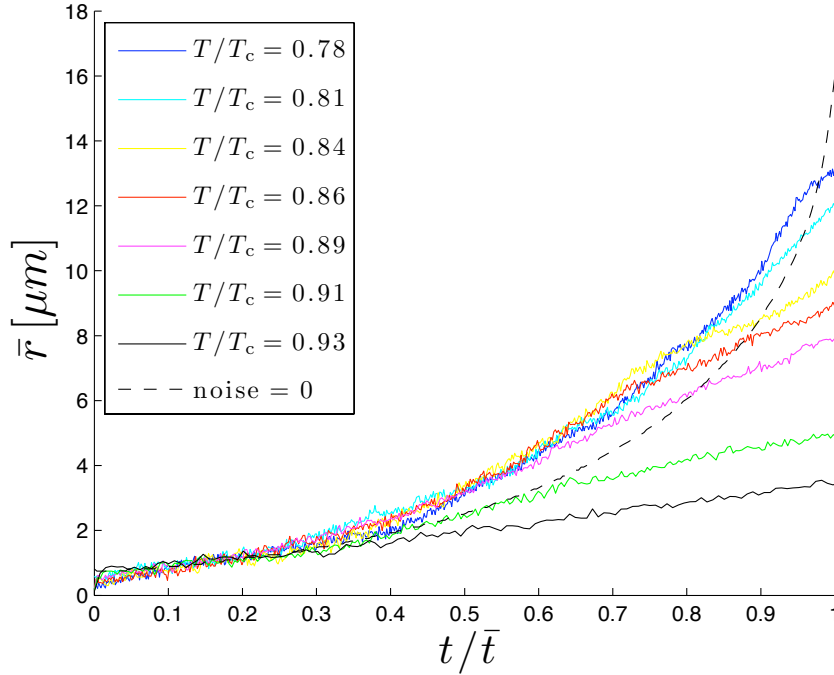


Figure 6.8: Mean vortex radius as a function of  $t/\bar{t}$ , where  $\bar{t}$  is the mean first exit time, for all temperatures in a system with an aspect ratio of 4:1 as found from an ensemble average of SGPE trajectories. The no noise case (dashed line) represents purely dissipative vortex decay.

## 6.4 Effects of Geometry

We performed the foregoing analysis for further condensate geometries based on aspect ratios of 1:1, 2:1 and 15:1, holding the geometric average constant at  $\bar{\omega} = 2\pi \times 19.73 \text{ s}^{-1}$  (5.6). Here we show the effect geometry has on vortex decay, while controlling all thermodynamic quantities by keeping  $\bar{\omega}$  constant.

### 6.4.1 Mean First Exit Time

Figure 6.9 shows that the mean first exit time decreases for higher temperatures for all geometries as expected. We see for the systems with an aspect ratio of 2:1 and 1:1, the mean exit time has the same linear relationship as observed with the 4:1 system. Note that the mean first exit time decreases as the system becomes spherical, consistent with the effect of Kelvin waves creating added instability. This is in contrast to the flattest case of 15:1 where although we see the exit time decrease, the relationship is not strictly linear as in the other geometries. For temperatures less than  $T/T_c = 0.86$  in the 15:1 dimensionality, the mean exit time is largest of all the geometries as expected as there will be less vortex bending in

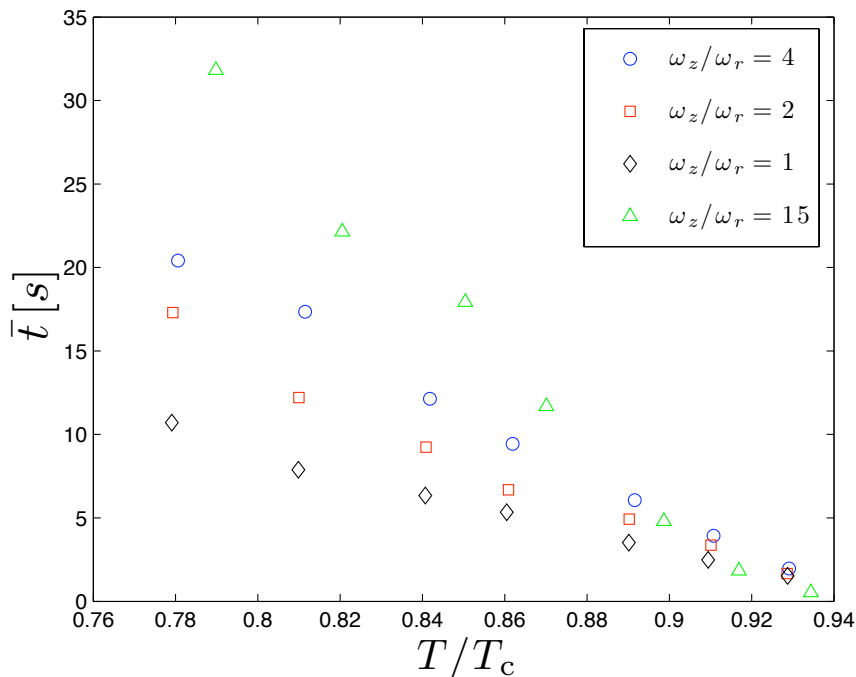


Figure 6.9: Mean first exit time as a function of temperature for the 4:1 (circle), 2:1 (square), 1:1 (diamond) and 15:1 (triangle) geometries with constant  $\bar{\omega}$ , in a system with  $5 \times 10^5$  total atoms. Note the similar linear relationship of the 4:1, 2:1 and 1:1 systems, while the 15:1 system has rather different behavior near  $T_c$ .

the flatter geometry. Also the decrease of the exit time is similar to the other geometries. However for the hotter temperatures we see signs of a transition into some new regime. The exit times are much faster than for the more spherical geometries, and the relationship is nonlinear.

To show the effect that geometry has on the mean first exit time in detail, it is convenient to look at the effective decay rate  $1/\bar{t}$  (see figure 6.10). We use the parameter  $\omega_r/\omega_z$ , since an increase in this variable corresponds to the system becoming more spherical in geometry. The three most spherical geometries corresponding to aspect ratios of 1:1, 2:1 and 4:1, show that the rate of vortex decay increases uniformly over all temperatures as the geometry becomes more spherical. This is consistent with Kelvin waves, leading to vortex bending for more spherical geometries and affecting the decay rate. In the most two dimensional geometry with aspect ratio of 15:1, the two regimes observed in figure 6.9 become very clear in figure 6.10. For the coldest temperatures less than  $T/T_c = 0.86$ , we see the vortex decay rate decrease in a very regular manner in comparison to the other geometries. The abnormal behavior of the hottest temperatures is clear as the vortex decay rate increases, in contrast to the expected decrease in rate for a vortex in a flatter condensate. The magnitude of this increased rate for the 15:1 geometry becomes larger as temperature increases. Note that in

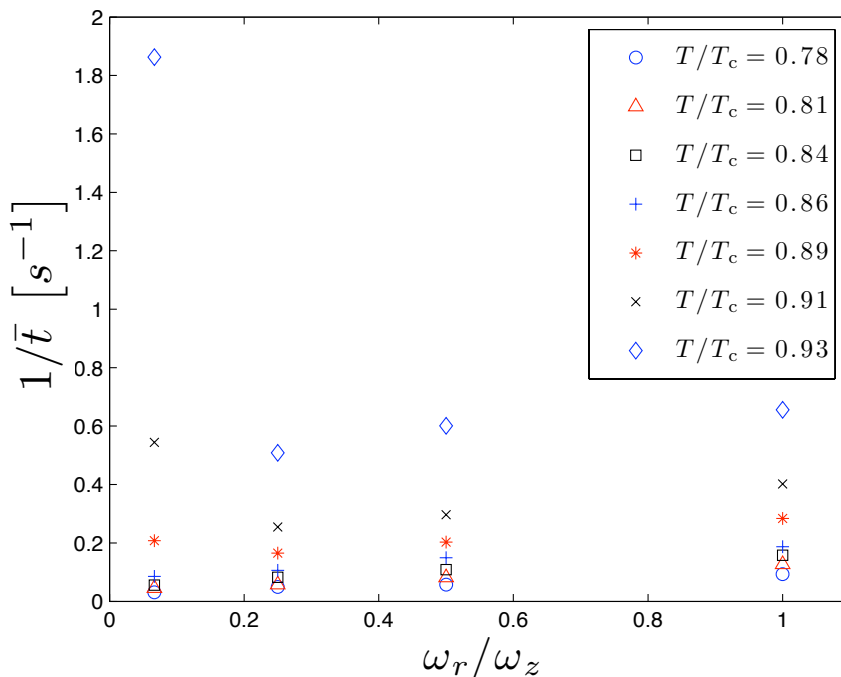


Figure 6.10: Effective vortex decay rate ( $1/\bar{t}$ ) as a function of  $\omega_r/\omega_z$ , where increasing this ratio corresponds to the geometry becoming more spherical. For the three most spherical geometries the decay rate increases as the condensate becomes more spherical showing evidence of vortex bending. The anomalous behavior of the 15:1 geometry is very clear in this figure.

all geometries, higher temperatures correspond to a larger decay rate, consistent with the increasing effect thermal fluctuations have at hotter temperatures.

## 6.4.2 Angular Momentum

The form of the angular momentum decay for the different geometries at a constant temperature is shown in figure 6.12, and is one of the most interesting results of this research. We observe that for a given temperature, the angular momentum decay for the 4:1, 2:1, and 1:1 geometries has the same form in units of the mean first exit time. For the cold temperature of  $T/T_c = 0.78$ , the angular momentum decay in the 15:1 geometry agrees well with the more spherical geometries. In contrast, we see for the high temperature of  $T/T_c = 0.93$  that the 15:1 geometry is much different. This is consistent with the vortex decay rate (figure 6.10) where the anomalous behavior for the 15:1 geometries was only observed for high temperatures. The fact that there is such universal angular momentum decay over the different geometries is quite surprising. This shows that although the actual vortex decay rate is faster as the dimensionality becomes more spherical, the structure of the decay is universal



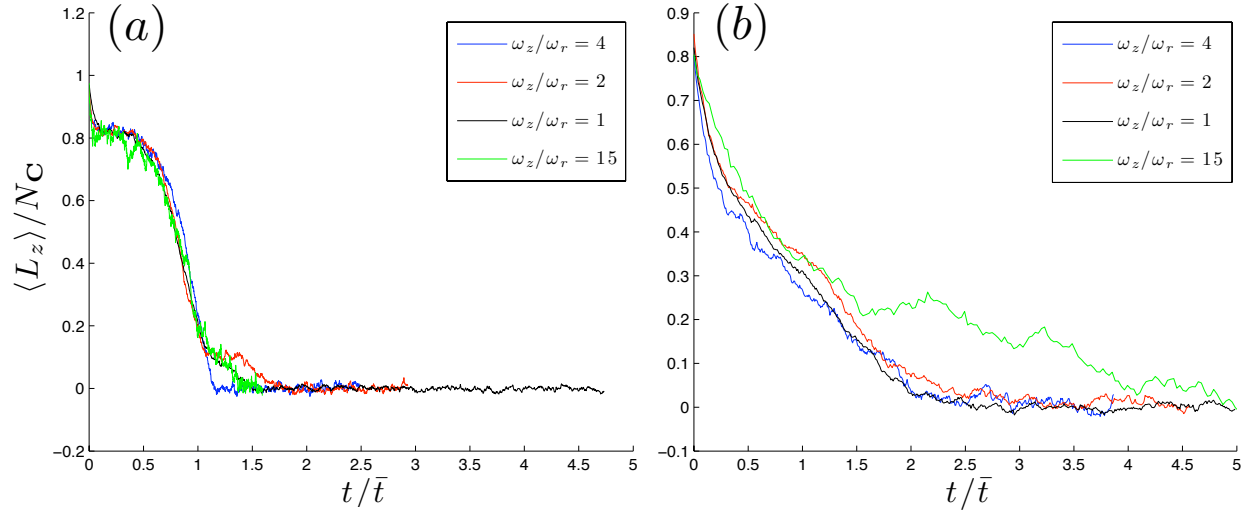


Figure 6.11: Decay of the  $z$  component of the angular momentum per particle as a function of  $t/\bar{t}$  for all geometries for fixed temperatures of (a)  $T/T_c = 0.78$ , and (b)  $T/T_c = 0.93$ . We see the decay is universal over all geometries in the colder temperature (a), while for the hotter case (b) we see it is universal, except for the 15:1 geometry (green) which shows a less clear decay than that observed in the more spherical geometries.

over geometry (excluding the anomalous 15:1 results).

### 6.4.3 Mean Vortex Radius

The effect of geometry on the mean vortex radius is shown in figure 6.12, where we see results consistent with the observations from the angular momentum decay. In figure 6.12 we use the length scale of  $\bar{r}/\bar{r}_{\max}$ , where  $\bar{r}_{\max}$  is the average vortex radius when the vortex becomes unobservable for each geometry, to account for the change in condensate size as geometry changes. Again for low temperature all curves have the same universal shape, while the unusual behavior of the vortex decay in the 15:1 geometry is clearly seen for  $T/T_c = 0.93$ . This shows again the universality that the form of the vortex decay has over geometry.

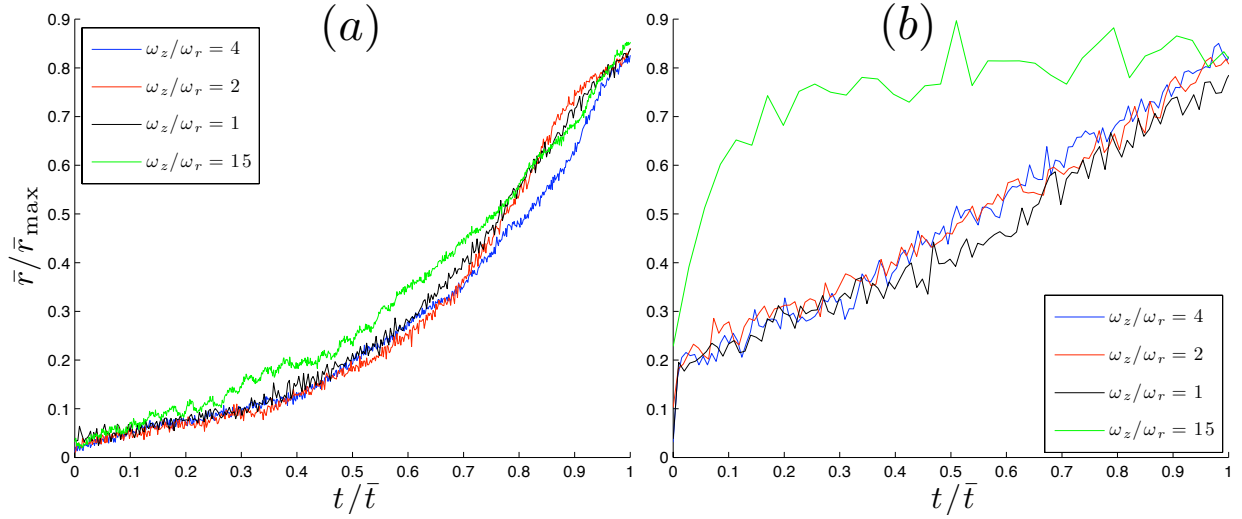


Figure 6.12: Mean vortex radius scaled by  $r_{\max}$  as a function of  $t/\bar{t}$  for all geometries for fixed temperatures of (a)  $T/T_c = 0.78$ , and (b)  $T/T_c = 0.93$ . We see (a) the universality of the mean vortex radius for the colder temperature. While in (b) the anomalous behavior of the 15:1 geometry (green) for hotter temperatures is clear.

#### 6.4.4 Temperature Dependence of All Geometries

Based on these results showing the universality of vortex decay over geometry, we can expect that the temperature dependence of the decay will be similar to that in the 4:1 geometry seen in section 6.3. We find for the 2:1 and 1:1 geometries, the angular momentum and radius of the single vortex is of the same form as figures 6.7 and 6.8. In the case of the 15:1 geometry, the corresponding curves are not as similar which is expected as we have seen some unusual behavior at this dimensionality. These results do not show any new physics but for completeness, we include the figures for the 1:1, 2:1 and 15:1 geometries corresponding to figures 6.7 and 6.8 in appendix A.

# Chapter 7

## Conclusion

### 7.1 Summary

We have considered the three dimensional dynamics of a single vortex in a Bose-Einstein condensate at high temperature where the effects of a thermal cloud are substantial. Using the simple growth SGPE (3.58), we have found that vortex dynamics are very complex and include both dissipative and diffusive dominated regimes of decay.

Our study involving a wide range of temperatures and geometries required prior knowledge of the simulation parameters in order to have a good control of the system. The work done in providing an accurate method for predicting SGPE parameters was central to this study. By knowing the parameters required to constrain the total number of atoms, we were able to investigate specific temperatures and compare a wide range of vortex decay processes.

Using our vortex detection scheme, we were able to define the mean first exit time for a single vortex. We saw that this time decreased as the temperature increased, showing that the presence of a larger thermal cloud will increase the decay rate. We found the mean first exit time for a fixed number of atoms decreased linearly with respect to temperature for all but the flattest geometries, which is interesting in its simplicity. As our vortex detection tracks the vortex until it becomes indistinguishable from fluctuations, it seem reasonable that it will correspond to experimental observations. It will be interesting to see if an experimental investigation into vortex lifetime in high temperature Bose-Einstein condensation gave a similarly simple relationship between lifetime and temperature.

The SGPE which accounts for both dissipative and diffusive dynamics, has shown that the form of vortex decay is very complex. We found that the SGPE can account for both dissipative and diffusive dominated decay, and that in general a combination of both processes are present in vortex decay. As temperature approaches the transition we see that diffusion dominates the decay, hence a description using a full stochastic theory is required. The observation of these complex dynamics is in contrast to the recent work by Jackson *et al.* [30], where they see little influence of fluctuations, and consider relatively low temperatures.

Possibly the most remarkable result of this work is that we have found the form of the vortex decay is universal over dimensionality for fixed temperature. This is despite finding

that faster decay rates occur for more spherical geometries, showing that Kelvin waves creating vortex bending modes do cause greater instability as the geometry becomes more spherical.

## 7.2 Directions for Future Research

This work has created the avenue for a large amount future work. The single vortex decay has not been fully accounted for, as the interesting effects of the 15:1 geometry have not been resolved. It will be interesting to see what the effects of a flatter, more two dimensional condensate will have on single vortex decay.

As we have found an effective way of choosing SGPE parameters which give excellent control of a system, the possibility of using the SGPE to perform similar studies in different systems is unlimited. A natural extension of this work will be applying a similar methodology to the case of a vortex dipole. The mechanism for dipole annihilation in high temperature Bose-Einstein condensates is an unresolved issue, so a full SGPE investigation would be of interest.

The methods we have derived for predicting SGPE parameters apply above the transition temperature as well. We have made the first steps in being able to make a fully quantitative investigation of the physics involved in crossing the transition, and to look in detail at the Kibble-Zurek mechanism.

In this research we used the simple growth SGPE (3.58) which did not include the scattering term. Once the scattering term has been implemented, this work will provide an interesting comparison to see if any extra details arise from using the full SGPE (3.50).

We have seen the SGPE show some fascinating results for the seemingly simple regime of single vortex decay. This work has made the first step in what is sure to be an exciting future for SGPE investigations in high temperature Bose-Einstein condensates.

# Appendix A

## Supplementary Figures

Here we present figures discussed in section 6.4.4., which show the angular momentum decay and mean vortex radius for the 1:1, 2:1 and 15:1 geometries. As expected from the results of section 6.4, we see that the 2:1 and 1:1 geometries agree well with the results for the 4:1 geometry, while the 15:1 geometry shows a different behavior.

## Appendix A. Supplementary Figures

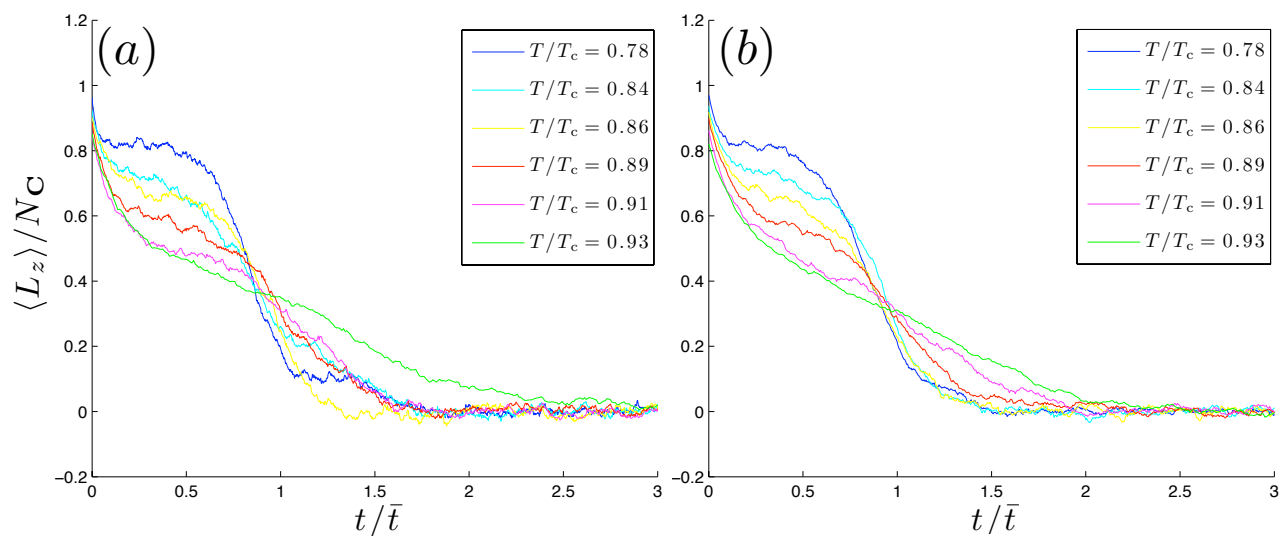


Figure A.1: Averaged z component of the angular momentum per particle as a function of  $t/\bar{t}$  for each temperature investigated, with a geometry of 2:1 (a) and 1:1 (b). These curves are of the same form as that for the 4:1 geometry (see figure 6.7).

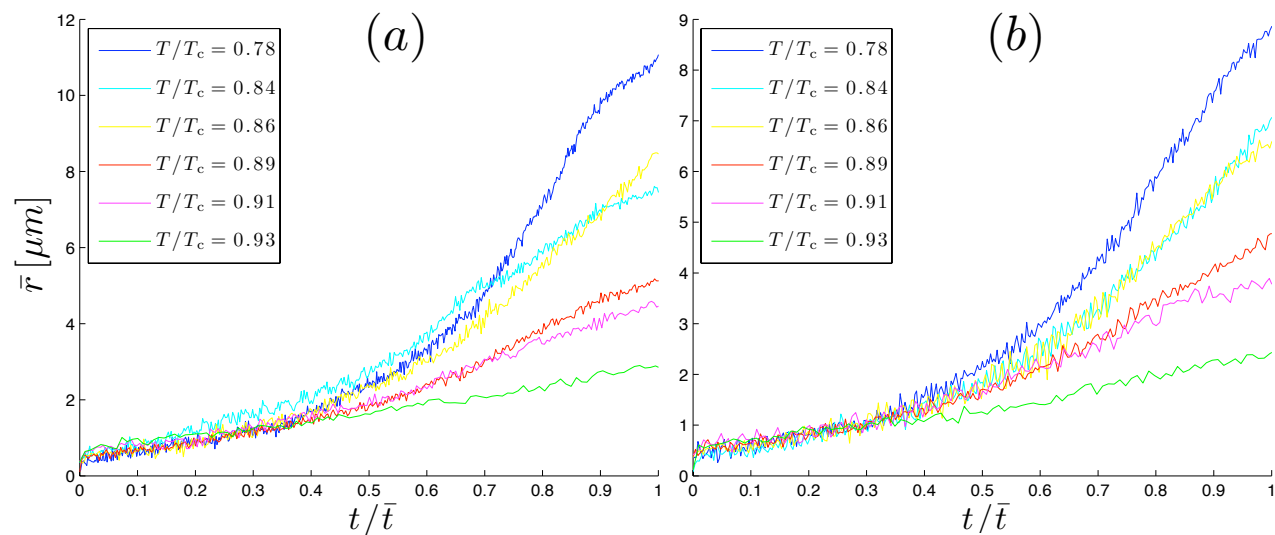


Figure A.2: Mean vortex radius as a function of  $t/\bar{t}$  for each temperature investigated. The two geometries are for an aspect ratio of 2:1 (a) and 1:1 (b). As with the angular momentum decay, these curves are of the same form as that for the 4:1 geometry (see figure 6.8).

## Appendix A. Supplementary Figures

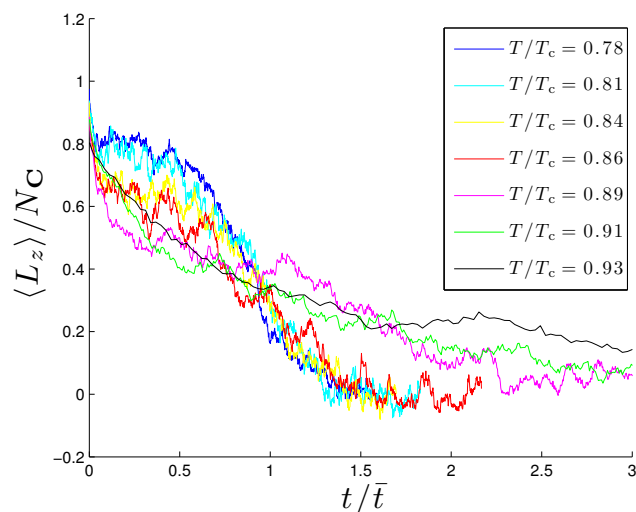


Figure A.3: Average of the z component of the angular momentum per particle as a function of  $t/\bar{t}$  for each temperature investigated, for a system with a 15:1 geometry. The low temperatures show some agreement with the corresponding case for the 4:1, 2:1 and 1:1 geometries (figures 6.7 and A.1), but all the curves are not very smooth and do not show the same clear differences in vortex decay.

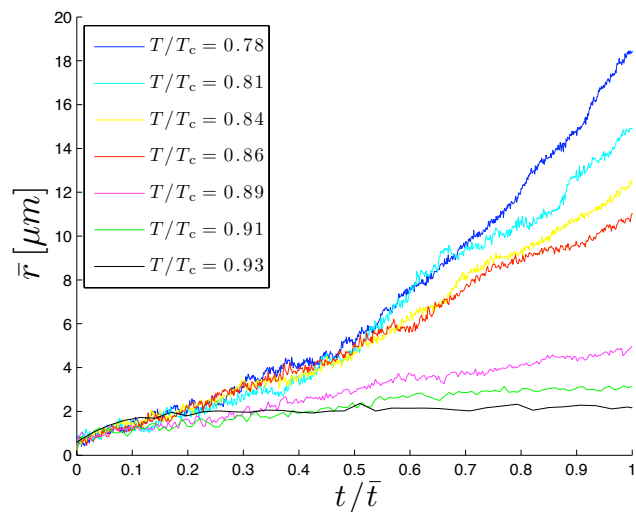


Figure A.4: Mean vortex radius as a function of  $t/\bar{t}$  for each temperature investigated, for a system with a 15:1 geometry. Here the low temperature curves are quite similar to the 4:1, 2:1 and 1:1 geometries (figures 6.8 and A.2), while the hotter temperatures show quite different behavior.

# Bibliography

- [1] B. P. Anderson, P. C. Haljan, C. E. Wieman, and E. A. Cornell. Vortex Precession in Bose-Einstein Condensates: Observations with Filled and Empty Cores. *Phys. Rev. Lett*, 85(14):2857–2860, 2000.
- [2] M. H. Anderson, J. R. Ensher, M. R. Matthews, C. E. Wieman, and E. A. Cornell. Observation of Bose-Einstein Condensation in a Dilute Atomic Vapor. *Science*, 269(5221):198–201, 1995.
- [3] M. J. Bijlsma, E. Zaremba, and H. T. C. Stoof. Condensate growth in trapped Bose gases. *Phys. Rev. A*, 62(6):063609, 2000.
- [4] P. B. Blakie. Numerical method for evolving the projected Gross-Pitaevskii equation. *Phys. Rev. E*, 78(2):026704, 2008.
- [5] P. B. Blakie, A. S. Bradley, M. J. Davis, R. J. Ballagh, and C. W. Gardiner. Dynamics and statistical mechanics of ultra-cold Bose gases using c-field techniques. *Advances in Physics*, 57(5):363 – 455, 2008.
- [6] P. B. Blakie and M. J. Davis. Projected Gross-Pitaevskii equation for harmonically confined Bose gases at finite temperature. *Phys. Rev. A*, 72(6):063608, 2005.
- [7] P. B. Blakie and M. J. Davis. Classical region of a trapped Bose gas. *J. Phys. B*, 40(11):2043–2053, 2007.
- [8] A. S. Bradley. *Theoretical Investigations of Trapped Ultra-Cold Bose Gases*. PhD thesis, Victoria University of Wellington, 2005.
- [9] A. S. Bradley and C. W. Gardiner. Diffusive instability of a vortex in a rotating Bose gas. *arXiv:cond-mat 0509592*, 2005.
- [10] A. S. Bradley and C. W. Gardiner. The stochastic Gross-Pitaevskii equation: III. *arXiv:cond-mat 0602162*, 2006.
- [11] A. S. Bradley, C. W. Gardiner, and M. J. Davis. Bose-Einstein condensation from a rotating thermal cloud: Vortex nucleation and lattice formation. *Phys. Rev. A*, 77(3):033616, 2008.



- [12] V. Bretin, P. Rosenbusch, F. Chevy, G. V. Shlyapnikov, and J. Dalibard. Quadrupole Oscillation of a Single-Vortex Bose-Einstein Condensate: Evidence for Kelvin Modes. *Phys. Rev. Lett*, 90(10):100403, 2003.
- [13] B. M. Caradoc-Davies. *Vortex Dynamics in Bose-Einstein Condensates*. PhD thesis, University of Otago, 2000.
- [14] F. Dalfovo, S. Giorgini, L. P. Pitaevskii, and S. Stringari. Theory of Bose-Einstein condensation in trapped gases. *Rev. Mod. Phys*, 71(3):463–512, 1999.
- [15] M. J. Davis. *Dynamics of Bose-Einstein Condensation*. PhD thesis, University of Oxford, 2001.
- [16] M. J. Davis, S. A. Morgan, and K. Burnett. Simulations of Bose Fields at Finite Temperature. *Phys. Rev. Lett*, 87(16):160402, 2001.
- [17] R. J. Donnelly. *Quantized Vortices in Helium II*. Cambridge University Press, 1991.
- [18] R. A. Duine, B. W. A. Leurs, and H. T. C. Stoof. Noisy dynamics of a vortex in a partially Bose-Einstein condensed gas. *Phys. Rev. A*, 69(5):053623, 2004.
- [19] R. A. Duine and H. T. C. Stoof. Stochastic dynamics of a trapped Bose-Einstein condensate. *Phys. Rev. A*, 65(1):013603, 2001.
- [20] P. O. Fedichev and G. V. Shlyapnikov. Dissipative dynamics of a vortex state in a trapped Bose-condensed gas. *Phys. Rev. A*, 60(3):R1779–R1782, 1999.
- [21] A. L. Fetter. Vortex Stability in a Trapped Bose Condensate. *J. Low Temp. Phys*, 113(3-4):189–194, 1998.
- [22] A. L. Fetter. Kelvin mode of a vortex in a nonuniform Bose-Einstein condensate. *Phys. Rev. A*, 69(4), 2004.
- [23] A. L. Fetter and A. A. Svidzinsky. Vortices in a trapped dilute Bose-Einstein condensate. *J. Phys. Cond. Mat*, 13(12):R135–R194, 2001.
- [24] C. W Gardiner. *Handbook of Stochastic Methods for Physics, Chemistry, and the Natural Sciences*. Springer, Berlin, 3rd ed edition, 2004.
- [25] C. W. Gardiner and M. J. Davis. The stochastic Gross-Pitaevskii equation: II. *J. Phys. B: At. Mol. Opt. Phys*, 36(23):4731–4753, 2003.
- [26] C. W. Gardiner and P. Zoller. Quantum kinetic theory: A quantum kinetic master equation for condensation of a weakly interacting Bose gas without a trapping potential. *Phys. Rev. A*, 55(4):2902–2921, 1997.
- [27] C. W. Gardiner and P. Zoller. Quantum kinetic theory III. Quantum kinetic master equation for strongly condensed trapped systems. *Phys. Rev. A*, 58(1):536–556, 1998.

- [28] C. W. Gardiner and P. Zoller. *Quantum Noise*. Springer, 2nd edition, 1999.
- [29] C. W. Gardiner and P. Zoller. Quantum kinetic theory V. Quantum kinetic master equation for mutual interaction of condensate and noncondensate. *Phys. Rev. A*, 61(3):033601, 2000.
- [30] B. Jackson, N. P. Proukakis, C. F. Barenghi, and E. Zaremba. Finite-temperature vortex dynamics in Bose-Einstein condensates. *Phys. Rev. A*, 79(5):053615, 2009.
- [31] E. Madarassy and C. Barenghi. Vortex Dynamics in Trapped Bose-Einstein Condensate. *J. Low Temp. Phys*, 152(3):122–135, 2008.
- [32] M. R. Matthews, B. P. Anderson, P. C. Haljan, D. S. Hall, C. E. Wieman, and E. A. Cornell. Vortices in a Bose-Einstein Condensate. *Phys. Rev. Lett*, 83(13):2498–2501.
- [33] A. A. Norrie. *A Classical Field Treatment of Colliding Bose-Einstein Condensates*. PhD thesis, University of Otago, 2005.
- [34] A. Penckwitt. *Rotating Bose-Einstein Condensates: Vortex Lattices and Excitations*. PhD thesis, University of Otago, 2003.
- [35] C. J. Pethick and H. Smith. *Bose-Einstein Condensation in Dilute Gases*. Cambridge University Press, 2002.
- [36] N. P. Proukakis and B. Jackson. Finite-temperature models of Bose-Einstein condensation. *J Phys B-At Mol Opt*, 41(20):203002, 2008.
- [37] H. Pu, C. K. Law, J. H. Eberly, and N. P. Bigelow. Coherent disintegration and stability of vortices in trapped Bose condensates. *Phys. Rev. A*, 59(2):1533–1537, 1999.
- [38] D. S. Rokhsar. Vortex Stability and Persistent Currents in Trapped Bose Gases. *Phys. Rev. Lett*, 79(12):2164–2167, 1997.
- [39] H. T. C. Stoof. Coherent Versus Incoherent Dynamics During Bose-Einstein Condensation in Atomic Gases. *J. Low Temp. Phys*, 114(1-2):11–108, 1999.
- [40] H. T. C. Stoof and M. J. Bijlsma. Dynamics of Fluctuating Bose-Einstein Condensates. *J. Low Temp. Phys*, 124(3-4):431–442, 2001.
- [41] C. N. Weiler, T. W. Neely, D. R. Scherer, A. S. Bradley, M. J. Davis, and Brian P. Anderson. Spontaneous vortices in the formation of Bose-Einstein condensates. *Nature*, 455(7215):948–951, 2008.
- [42] E. Wigner. On the Quantum Correction For Thermodynamic Equilibrium. *Phys. Rev*, 40(5):749–759, 1932.
- [43] E. Zaremba, T. Nikuni, and A. Griffin. Dynamics of Trapped Bose Gases at Finite Temperatures. *J. Low Temp. Phys*, 116(3):277–345, 1999.